The Astrophysical Journal, 837:125 (22pp), 2017 March 10 https://doi.org/10.3847/1538-4357/aa603e

Hydrogen Balmer Line Broadening in Solar and Stellar Flares

Adam F. Kowalski[1,2], Joel C. Allred[3], Han Uitenbroek[2], Pier-Emmanuel Tremblay[4], Stephen Brown[5], Mats Carlsson[6], Rachel A. Osten[7], John P. Wisniewski[8], and Suzanne L. Hawley[9]
[1] Department of Astrophysical and Planetary Sciences, University of Colorado Boulder, 2000 Colorado Avenue, Boulder, CO 80305, USA; Adam.Kowalski@lasp.colorado.edu
[2] National Solar Observatory, University of Colorado Boulder, 3665 Discovery Drive, Boulder, CO 80303, USA
[3] NASA/Goddard Space Flight Center, Code 671, Greenbelt, MD 20771, USA
[4] Department of Physics, University of Warwick, Coventry CV47AL, UK
[5] School of Physics and Astronomy, Kelvin Building, University of Glasgow, G12 8QQ, UK
[6] Institute of Theoretical Astrophysics, University of Oslo, P.O. Box 1029 Blindern, NO-0315 Oslo, Norway
[7] Space Telescope Science Institute, 3700 San Martin Drive, Baltimore, MD 21218, USA
[8] Homer L. Dodge Department of Physics and Astronomy, University of Oklahoma, 440 W. Brooks Street, Norman, OK 73019, USA
[9] University of Washington Department of Astronomy, 3910 15th Avenue NE, Seattle, WA 98195, USA
Received 2016 December 19; revised 2017 February 6; accepted 2017 February 9; published 2017 March 10

Abstract

The broadening of the hydrogen lines during flares is thought to result from increased charge (electron, proton) density in the flare chromosphere. However, disagreements between theory and modeling prescriptions have precluded an accurate diagnostic of the degree of ionization and compression resulting from flare heating in the chromosphere. To resolve this issue, we have incorporated the unified theory of electric pressure broadening of the hydrogen lines into the non-LTE radiative-transfer code RH. This broadening prescription produces a much more realistic spectrum of the quiescent, A0 star Vega compared to the analytic approximations used as a damping parameter in the Voigt profiles. We test recent radiative-hydrodynamic (RHD) simulations of the atmospheric response to high nonthermal electron beam fluxes with the new broadening prescription and find that the Balmer lines are overbroadened at the densest times in the simulations. Adding many simultaneously heated and cooling model loops as a "multithread" model improves the agreement with the observations. We revisit the three-component phenomenological flare model of the YZ CMi Megaflare using recent and new RHD models. The evolution of the broadening, line flux ratios, and continuum flux ratios are well-reproduced by a multithread model with high-flux nonthermal electron beam heating, an extended decay phase model, and a "hot spot" atmosphere heated by an ultrarelativistic electron beam with reasonable filling factors: ∼0.1%, 1%, and 0.1% of the visible stellar hemisphere, respectively. The new modeling motivates future work to understand the origin of the extended gradual phase emission.

Key words: methods: numerical – radiative transfer – stars: atmospheres – stars: flare – Sun: atmosphere – Sun: flares

1. Introduction

In the standard flare model, coronal magnetic energy is converted to the kinetic energy of particles, which heats the chromosphere and increases the ambient charge density. This increased charge density results from direct nonthermal ionizations from the impacting flare-accelerated particles as well as thermal ionizations in the heated and compressed chromosphere from shock fronts generated by these nonthermal particles. Determining the charge density in the chromosphere from observed spectra therefore provides a way to critically test the predictions of the proposed flare energy transport and heating mechanisms, such as particle beams (Brown 1971; Hawley & Fisher 1994; Abbett & Hawley 1999; Allred et al. 2005), conduction (Longcope 2014), and Alfvén waves (Fletcher & Hudson 2008; Russell & Fletcher 2013; Reep & Russell 2016). The charge density is a fundamental physical parameter of flare atmospheres and has many important effects on the emergent flare spectra through the recombination and bound–bound emissivity, collisional rates, and the pressure broadening of lines. An accurate prescription for the atomic physics resulting from increased charge density in a realistic (stratified) flare atmosphere is critical for robust constraints on these heating mechanisms.

The charge density is detectable in spectra through the symmetric broadening of hydrogen or hydrogenic-like ions caused by electric microfield pressure broadening from ambient electrons and protons.[10] The local electric microfield breaks the degeneracy of the orbital angular momentum states, l, of each principal quantum number, n. In both solar and stellar flares, the broadening of the hydrogen Balmer lines has often been attributed to electric pressure broadening (Svestka 1963; Worden et al. 1984; Hawley & Pettersen 1991; Johns-Krull et al. 1997; Allred et al. 2006; Paulson et al. 2006; Gizis et al. 2013), but in some flares the role of electric pressure broadening is not clear and instead directed mass flows or a large turbulent broadening is favored (Doyle et al. 1988; Phillips et al. 1988; Eason et al. 1992; Fuhrmeister et al. 2011). It is important to accurately model the electric pressure broadening to better constrain the role of other broadening mechanisms and to better understand the Balmer edge spectral region ($\lambda = 3646$–3800 Å), where during flares, the wings of the broadened higher order lines merge (Donati-Falchi et al. 1985; Kowalski et al. 2015b).

[10] This is referred to as the linear Stark effect. We use "electric pressure broadening" to refer to the linear Stark effect in hydrogen or hydrogenic ions caused by electric microfields from the surrounding distribution of electrons and protons.

Various theoretical frameworks have been developed for electric pressure broadening profiles (Kepple & Griem 1968; Vidal et al. 1970, 1973). These are convolved with the line profile (typically a Voigt) function that includes thermal and natural broadening to obtain a total line absorption coefficient (Mihalas 1978; Tremblay & Bergeron 2009). Profile convolution is computationally demanding, and analytic approximations to the true electric pressure broadening profiles were presented by Sutton (1978; hereafter, S78) who derived a broadening parameter that is added as a damping term in the Voigt profile (Švestka & Fritzová-Švestková 1967), thus significantly decreasing the computational time in radiative-transfer codes. This modeling method has been shown to be adequate for the infrared lines of hydrogen in the non-flaring solar atmosphere (Carlsson & Rutten 1992) and has been used widely in modeling flare atmospheres (e.g., Kowalski et al. 2015b). The analytic approximations also have the benefit of being extended to any arbitrary high-order hydrogen line, whereas the "exact" (theoretical) profiles are usually only available for a limited number of transitions. However, for the regime of flare chromospheric densities ($n_e \gtrsim 10^{13}\,\mathrm{cm}^{-3}$; Worden et al. 1984; Donati-Falchi et al. 1985; García-Alvarez et al. 2002; Paulson et al. 2006; Kowalski et al. 2017), there is known to be a significant discrepancy between the analytic and theoretical profiles, resulting in an order of magnitude ambiguity for the inferred charge density (see Johns-Krull et al. 1997 for an extensive discussion). The analytic (S78) results are currently employed as Voigt profile damping parameters in several radiative-transfer codes. Notable among these are RH (Uitenbroek 2001), MULTI (Carlsson 1986), and the RADYN flare code (Allred et al. 2015). In this paper, we modify the RH code to include the theoretical electric pressure broadening line profiles from the unified theory of Vidal et al. (1970, 1971, 1973). We show how new calculations from snapshots of dynamic flare simulations result in a significant improvement on the inferred charge density regime that is relevant for flare chromospheres.

In Section 2, we describe the electric pressure broadening theory as implemented in the RH code and compare to the analytic approximations of the line profile function. In Section 3, we show how the new broadening profiles adequately reproduce the line broadening observed in the spectrum of Vega. In Section 4, we present improved hydrogen Balmer line broadening calculations from flare simulations with high-flux electron beams that were calculated with the RADYN code, and we analyze the predictions of the new theory for the relative fluxes in each Balmer line (the Balmer decrement). In Section 5, we compare the new broadening predictions to the spectra of the YZ CMi Megaflare and present a revised interpretation of the emission components using the spatial development of a large X-class solar flare. In Section 6, we discuss implications for the flare heating mechanisms and avenues for future work with the new hydrogen line broadening profiles. In Section 7, we summarize our conclusions. In Appendix A, we present the details of two new radiative-hydrodynamic flare models that are used in the analysis. In Appendix B, we list abbreviations and terminology.

2. Method

We model electric pressure broadening using the unified theory developed by Vidal et al. (1971, 1973; hereafter, VCS) and using the extended tables calculated by Tremblay & Bergeron (2009). Briefly, the unified theory accounts for perturbations from slowly moving (quasi-static) protons and the fast moving (dynamic) electrons with an accurate treatment of electron perturbations from line core to the wing. Vidal et al. (1973) provided electric pressure broadening line profiles for the lower order transitions of hydrogen, and Tremblay & Bergeron (2009; see also Lemke 1997) extended the Vidal et al. (1973) line profile function for electric pressure broadening, $S(\alpha)$, for transitions among 22 levels in the hydrogen Lyman, Balmer, Paschen, and Brackett series as a function of temperature and electron density.

We also include the non-ideal, bound–bound, and bound–free opacity modifications from level dissolution following the prescription in Hummer & Mihalas (1988), Dappen et al. (1987), and Tremblay & Bergeron (2009). This modeling prescription has been included in the RH code for calculations of the Balmer edge wavelength region for flares (Kowalski et al. 2015b). In this prescription, each level of hydrogen is assigned an occupational probability, w_n (see also Hubeny et al. 1994), which is the probability that the level is broadened by a critical electric microfield β_{crit} for level n and overlaps in energy with (broadened) higher energy levels. At $\beta \geqslant \beta_{\mathrm{crit}}$, ionization[11] can occur that results in the extension of the continuum opacity longward of the ionization limit. This extended continuum opacity is often referred to as the "pseudo-continuum" opacity (Dappen et al. 1987; Hubeny et al. 1994; Tremblay & Bergeron 2009). As a result level dissolution, bound–free Balmer continuum flux is observed at wavelengths longer than the edge wavelength, and the higher order Balmer lines are fainter than without level dissolution. The opacity effects from level dissolution produce model spectra that are generally consistent with the continuous flux observed at $\lambda = 3646$–3700 Å, the dissolved higher order lines from $\lambda = 3700$–3800 Å, and the blended wing flux between Balmer lines from 3700 to 3900 Å in dMe flare spectra in the literature. The amount by which the higher order Balmer lines dissolve (fade) into continuum flux complements the diagnostics of the ambient flare charge density provided by the broadening of the lower order Balmer lines (Kowalski et al. 2015b).

Tremblay & Bergeron (2009) modified the 10 Balmer and Lyman calculations of VCS using β_{crit} as an upper limit in both the electronic broadening profile and the renormalization integral of $S(\alpha)$, because higher microfield strengths $>\beta_{\mathrm{crit}}$ have a significant probability to transform bound–bound opacity into bound–free opacity (Seaton 1990). This makes the line broadening theory fully consistent with the independent Hummer & Mihalas (1988) equation of state. We have calculated the Balmer and Lyman lines up to H20, and for 19 Paschen lines and 10 Brackett lines using β_{crit} (see Equation (18) of Tremblay & Bergeron 2009). Hereafter, we refer to these profiles calculated with the VCS unified theory extended with the modifications of Tremblay & Bergeron (2009), the occupational probability formalism of Hummer & Mihalas

[11] The ionization that results from level dissolution is non-degenerate pressure broadening ionization, and experiments with sodium have demonstrated that ionization occurs at $\beta \geqslant \beta_{\mathrm{crit}}$ (Pillet et al. 1983, 1984; Arakelyan et al. 2016). On the microscopic level, a Landau–Zener (L–Z) transition (Zener 1932) can occur between the dissolved levels n and $n+1$ and rapidly proceed until the hydrogen atom is ionized (Rubbmark et al. 1981; Pillet et al. 1984; Hummer & Mihalas 1988; Stoneman et al. 1988); the L–Z transitions between dissolved energy levels of n and $n+1$ occur at "avoided crossings" (e.g., see the Quantum Picture described in Perotti 2006).

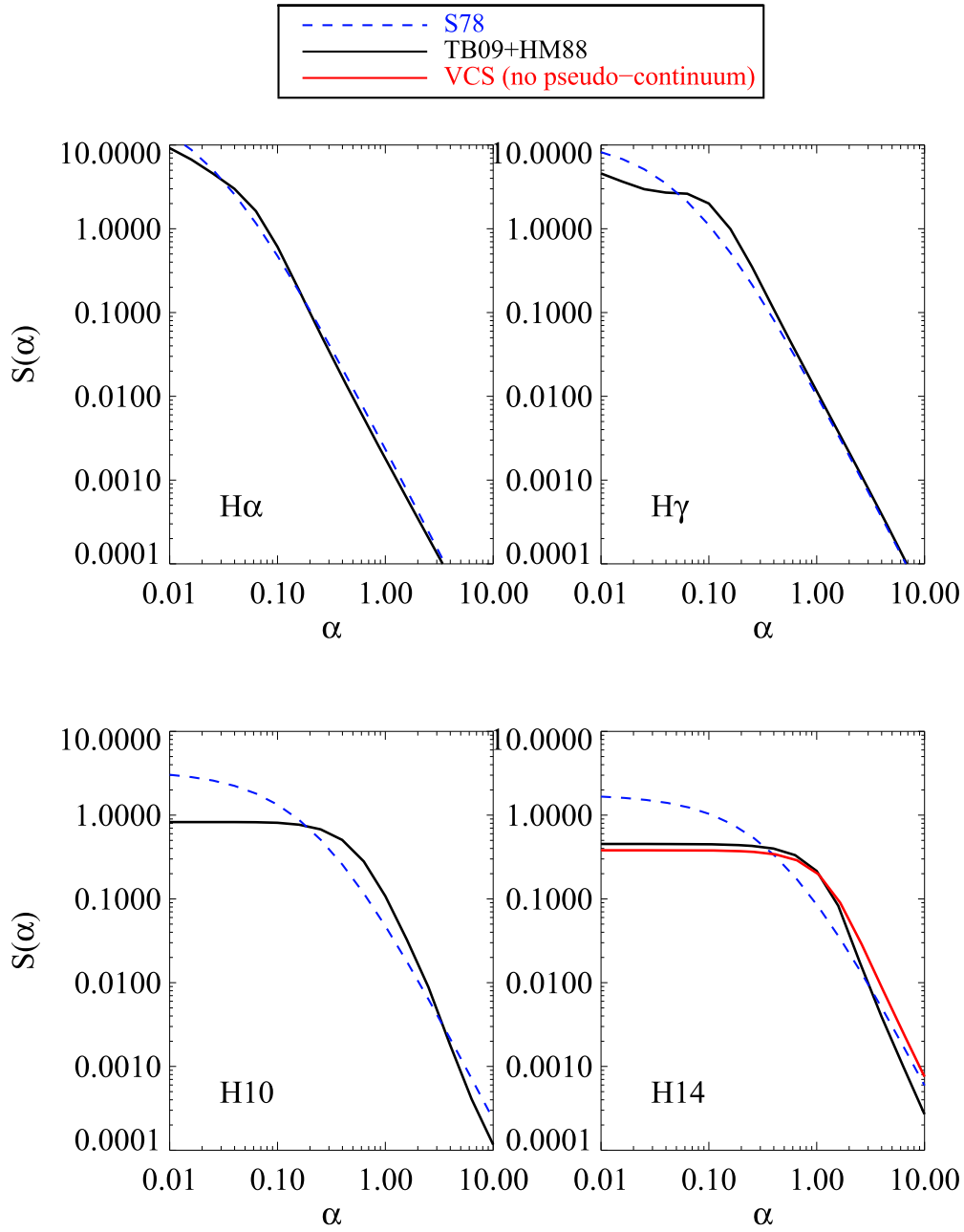

Figure 1. Electric pressure broadening profiles $S(\alpha)$ comparing the S78 method (dashed blue) and the TB09+HM88 method (solid black) for select Balmer lines. α is proportional to $\lambda - \lambda_o$; the conversion from α to $\Delta\lambda$ in Å is $1.25 \times 10^{-9} \times n_e^{2/3} = [0.58, 2.69, 12.5, 37]$ for $n_e = [10^{13}, 10^{14}, 10^{15}, 5 \times 10^{15}]$ cm^{-3}. These profiles use a temperature of $T = 10{,}000$ K and $n_e = 10^{14}$ cm^{-3}. The H14 profile (solid red) is the VCS profile of H14 from Lemke (1997) that does not account for level dissolution ($\beta_{\rm crit}$ is not used in the line profile calculation; see the text here and Tremblay & Bergeron 2009).

(1988), and the non-ideal (pseudo-continuum) opacity of Dappen et al. (1987) as the TB09+HM88 profiles.

In Figure 1, we plot several of the TB09+HM88 Balmer line profiles and compare them with the corresponding line profiles from S78 (Method #1), where $\alpha = (\lambda - \lambda_o)/F_o$ (λ is expressed in Å) and F_o is the field strength at the average interparticle separation. The conversion from α to $\Delta\lambda$ in Å is $F_o = 1.25 \times 10^{-9} \times n_e^{2/3} = [0.58, 2.69, 12.5, 37]$ for $n_e = [10^{13}, 10^{14}, 10^{15}, 5 \times 10^{15}]$ cm^{-3}. The VCS (no pseudo-continuum) profiles $S(\alpha)$ for different values of n_e generally overlap, and the comparisons to the S78 profiles were discussed in S78 for the lower order Balmer lines. Here we show the comparisons to the TB09+HM88 profiles only for $n_e = 10^{14}$ cm^{-3}, which demonstrates that the entire profile for Hα is well-reproduced by the S78 approximations and that the asymptotic Holtsmark profile ($\propto \alpha^{-5/2}$) is well-reproduced for the Hγ line. However, for the higher order Balmer line profiles (H10, H14) in Figure 1 the discrepancy becomes large (see also Figure 7 of Johns-Krull et al. (1997), for a comparison of other electric pressure broadening theories to S78 for H10). We show the H14 profile calculated with $\beta_{\rm crit}$ compared to the profile from Lemke (1997) without using $\beta_{\rm crit}$ (VCS, no pseudo-continuum). For larger electron densities, the discrepancy between the VCS (no pseudo-continuum) H14 profile and the TB09+HM88 H14 profile is even larger, as expected (Tremblay & Bergeron 2009).

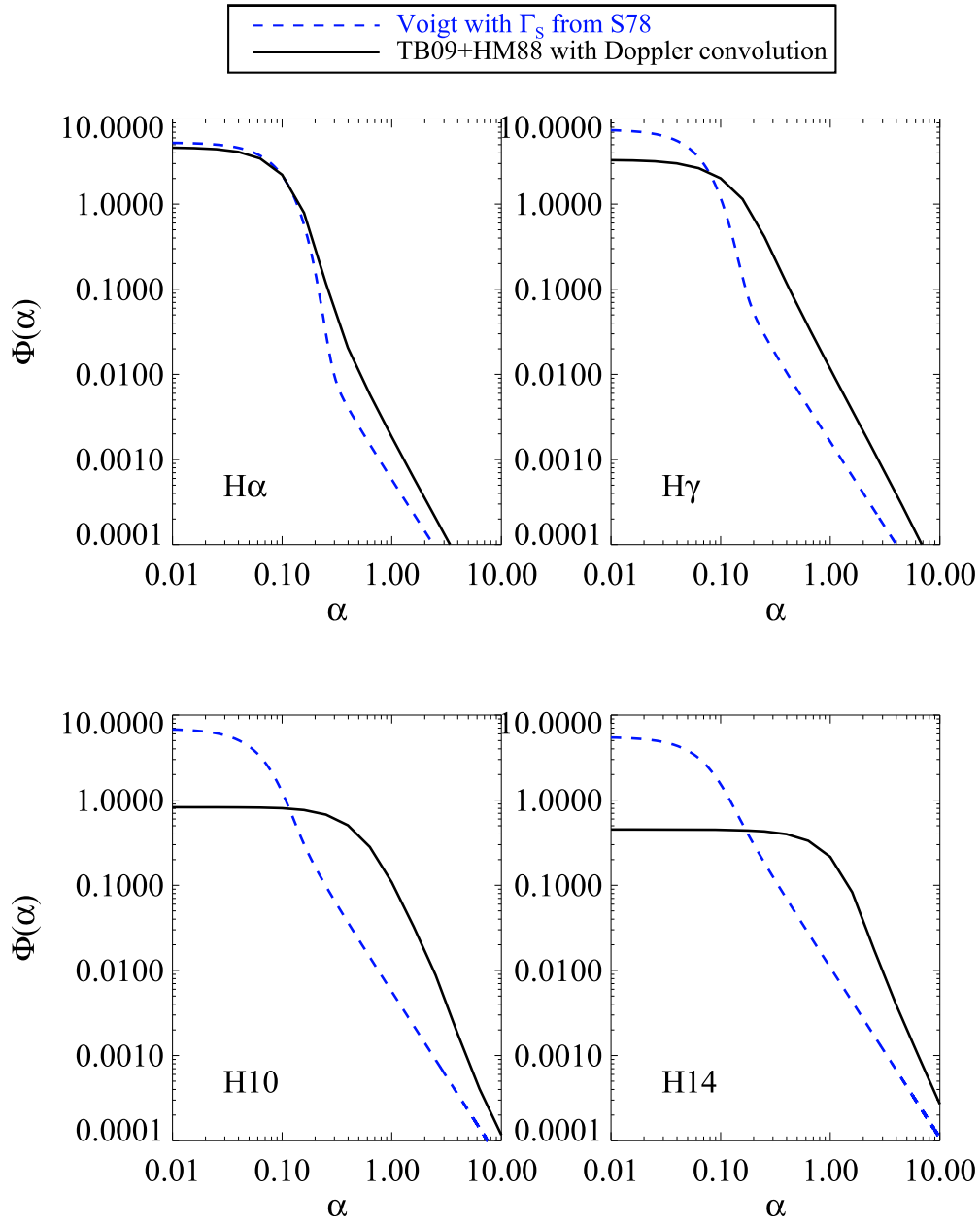

Figure 2. Line profiles $\Phi(\alpha)$ comparing the Voigt function with Γ_S obtained from S78 (dashed blue) to the TB09+HM88 profiles with Doppler convolution (solid black) for select Balmer lines. α is proportional to $\lambda - \lambda_o$; the conversion from α to $\Delta\lambda$ in Å is $1.25 \times 10^{-9} \times n_e^{2/3} = [0.58, 2.69, 12.5, 37]$ for $n_e = [10^{13}, 10^{14}, 10^{15}, 5 \times 10^{15}]$ cm^{-3}. These profiles use a temperature of $T = 10{,}000$ K and $n_e = 10^{14}$ cm^{-3}. The TB09+HM88 profiles have been calculated with $\beta_{\rm crit}$ as described in Tremblay & Bergeron (2009). The line profile functions largely differ for the two methods in the far wings of all Balmer lines and in the wings and cores for the Balmer lines that are of higher orders than Hα.

The analytic approximations from S78 are often used to estimate an electric pressure damping parameter, Γ_S, that is added to the total damping parameter in the Voigt profile (H), which dramatically decreases computational time and increases flexibility in radiative-transfer codes since an S78 profile can be calculated for a transition with any arbitrarily large upper principal quantum level. In Figure 2, we plot the normalized line profile function $\Phi(\alpha)$ for several Balmer lines using a Voigt function with Γ_S from S78 in the Voigt profile ($\Phi(\alpha) \propto H(\Gamma_{\rm tot} = \Gamma_{\rm tot} + \Gamma_S)$) compared to the TB09+HM88 line profile functions with a Doppler convolution ($\Phi(\alpha) \propto S(\alpha) * H$). We use $T = 10{,}000$ K for Doppler broadening in this comparison. Here it is most striking that using Γ_S in the Voigt profile does not adequately produce the broadening in the Balmer lines as predicted by the TB09 +HM88 profiles.

We modified the RH radiative-transfer code to convolve the Voigt function (with thermal and natural broadening) with the TB09+HM88 profiles ($S(\alpha)$), following Mihalas (1978) and Tremblay & Bergeron (2009) to obtain the normalized line profile function:

$$\Phi(\alpha) = \frac{d\nu}{d\alpha} \int_{-\infty}^{\infty} S^*(\Delta\nu + v\Delta\nu_D) H(a, v)\, dv \qquad (1)$$

where S^* is $S(\alpha)$ converted to frequency units and normalized to 1 from $-\infty$ to $+\infty$.

For the model atmospheres calculated in this work, we use a 20 level hydrogen model atom with the TB09+HM88 profiles

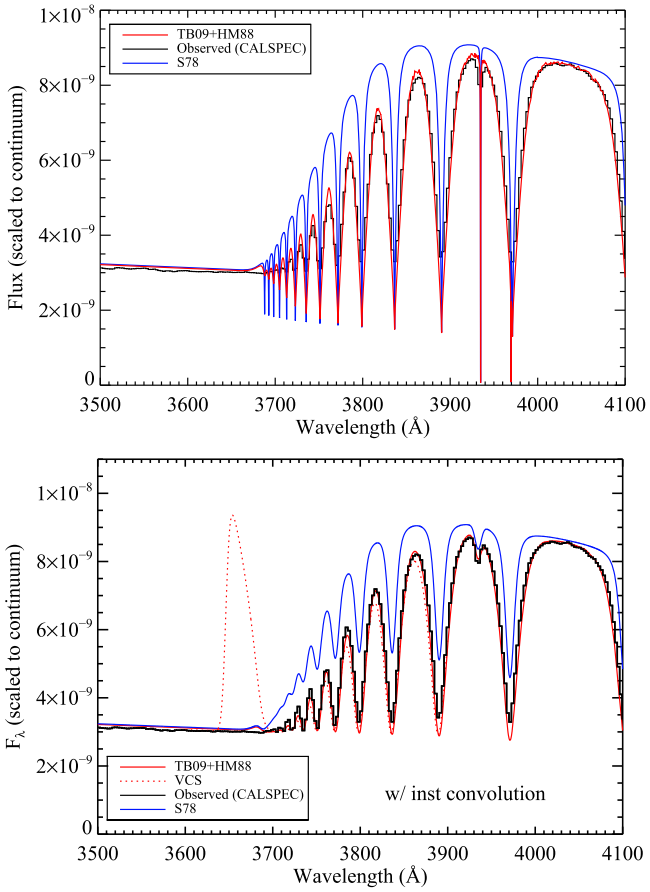

Figure 3. (Top) Observed spectrum of the A0 star, Vega, (black line) compared to predicted spectra using the S78 method (blue line) and the TB09+HM88 method (red line) from $\lambda = 3500$–4100 Å. (Bottom) The model spectra in the top panel have been convolved by the instrumental resolution of FWHM = 8 Å. The TB09+HM88 prescription for broadening and level dissolution (solid red) better accounts for the broadening and depth of the hydrogen Balmer lines. The dotted line shows the prediction using the VCS profiles without the bound–bound and bound–free opacity effects from level dissolution (no pseudo-continuum).

for the Balmer and Paschen lines as well as the opacity effects from level dissolution at the Balmer and Paschen edges. We also use a five-level Ca II model ion + continuum in the non-LTE calculation.[12] The Ca II H and K lines are important to include for a detailed assessment of the blending of the hydrogen line wings from $\lambda = 3900$–4000 Å.

3. Comparisons to Vega

To test our method, we compare observations of Balmer line flux from the A0 star, Vega, with simulated spectra produced from RH using our method and that of S78. The observations of Vega are described in Bohlin & Gilliland (2004) and Bohlin (2007) and were obtained from the Space Telescope Science Institute CALSPEC Calibration database. We have chosen Vega as a test case because it is a well-studied star with a known atmospheric structure and electron densities in the region of Balmer line formation that are similar to those previously inferred in flaring chromospheres. We input the atmospheric structure of Vega obtained from the ATLAS9 grid (Castelli & Kurucz 1994, 2004) into RH. Figure 3 shows the results of this comparison (where the bottom panel shows the effect of instrumental convolution). The black line is the observed spectrum, and the red and blue lines are the simulated spectra using our method with the TB09+HM88 profiles and the method of S78, respectively. Clearly, the TB09+HM88 prescription for broadening and level dissolution produces a much better fit to the observed spectrum at $\lambda \gtrsim 3700$ Å.

The TB09+HM88 broadening has been shown to accurately reproduce the CALSPEC spectra of Vega and white dwarfs using other radiative-transfer codes (Bohlin et al. 2014). Vega is a rapidly rotating star that is seen nearly pole-on (Aufdenberg et al. 2006). We do not include the projected rotational velocity, which broadens only the line core region. We investigate the effect on the wing broadening from the pole-to-limb variation of effective temperature ($\Delta T_{\rm eff} \sim 2200$ K) using the ATLAS9 grid. A model with $T_{\rm eff} = 10{,}250$ K at $\mu = 0.95$ (representative of the pole), together with a model with $T_{\rm eff} = 8000$ K at $\mu = 0.05$ (representative of the limb), does not improve the broadening produced by the S78 prescription.

As described in Section 2, we included the prescription from Dappen et al. (1987) for bound–bound and bound–free opacity effects due to hydrogen level dissolution into RH with the TB09+HM88 profiles.[13] In Figure 3 (top), the Balmer lines from S78 are narrower than with the VCS theory as implemented in the TB09+HM88 profiles, and the blending of the wings of the Balmer lines between $\lambda = 3700$–3950 Å is not nearly as prominent as the calculations with the TB09 +HM88 profiles, which result in deeper absorption and more blending in the wings even when instrumental resolution is incorporated (bottom panel of Figure 3). Both prescriptions produce bona-fide Balmer continuum flux longward of the Balmer limit at $\lambda = 3646$ Å.

In the bottom panel of Figure 3, the red dotted line shows the calculation without the opacity effects from level dissolution. Specifically, we set the occupational probability of each level n for hydrogen equal to one, we set the Balmer opacity longward of the Balmer limit to zero (no pseudo-continuum), and we use the VCS line broadening profiles from Lemke (1997) which do not include $\beta_{\rm crit}$ in the calculation of the line profile shape. We refer to this calculation as the "VCS (no pseudo-continuum)." The difference between this calculation compared to the observation at $\lambda \sim 3650$–3690 Å demonstrates that the bound–free opacity from level dissolution (the pseudo-continuum opacity) is necessary to accurately account for the continuum flux at these wavelengths even with the deep absorption and large broadening produced by the TB09 +HM88 profiles. For the charge density that produces the broadening in Vega, the Balmer bound–free opacity at wavelengths longward of the Balmer limit generally follows the trend in the flux between the Balmer lines in the S78 emergent flux spectrum at $\lambda = 3700$–3850 Å in Figure 3 (top). At these wavelengths in the TB09+HM88 prediction, the dominant opacity is the superposition of the bound–bound opacities of the hydrogen lines,[14] which causes the calculation

[12] We use the Ca II model that comes with the standard RH distribution. The only modification that is necessary is to extend the wavelength grid to cover the far wings of Ca II H and K.

[13] In Kowalski et al. (2015b), the same prescription with the S78 electric pressure broadening for flare model atmosphere calculations with the RH and RADYN codes was used.

[14] The TB09+HM88 profiles are calculated using $\beta_{\rm crit}$ because of the level dissolution from ambient protons; the profiles extend to infinity because the level dissolution from electrons does not have a sharp cutoff (see the discussion in HM88 and Tremblay & Bergeron 2009).

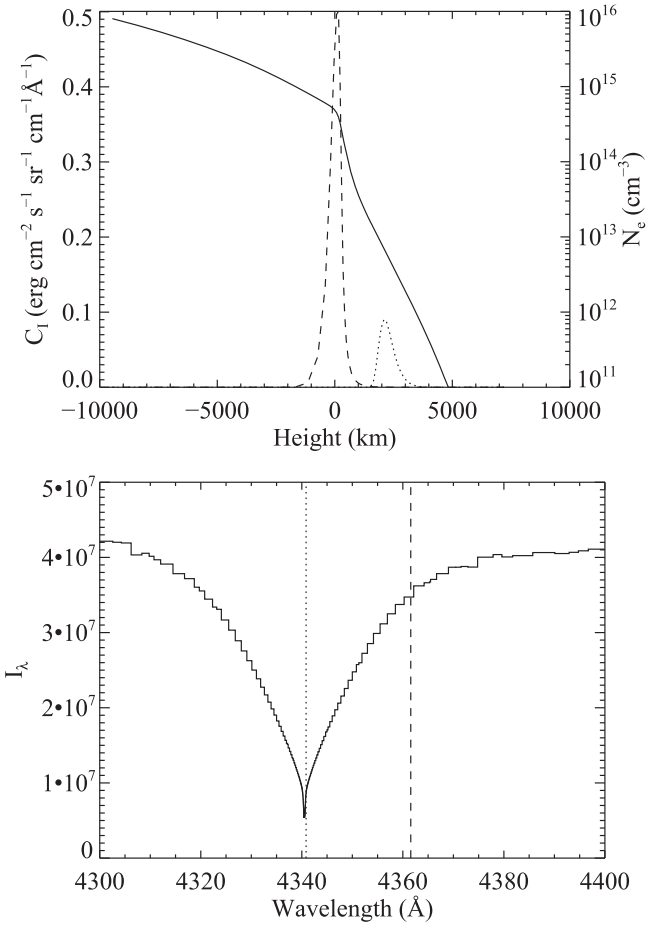

Figure 4. (Top panel) Contribution function plotted as a function of height above the photosphere for two representative wavelengths in the Hγ line. These are at line center (dotted line) and in the far wing at $\lambda_{\rm rest}$ + 20 Å (dashed line). The electron density (solid line) measured from the right axis is also plotted. (Bottom panel) The Hγ line profile with dotted and dashed lines indicating the wavelengths where the corresponding contribution functions are calculated. The line forms over a large range of electron density and the emergent spectrum is a combined intensity profile over a large range of electric pressure broadening amounts.

with the TB09+HM88 profiles and the calculation with the VCS (no pseudo-continuum) profiles to be similar at these wavelengths but with broader higher order line profiles in the latter (Tremblay & Bergeron 2009). The level dissolution opacity (i.e., that which is often referred to as the pseudo-continuum opacity) is most critical for reproducing the flux of Vega at λ between 3646 and 3700 Å, where the oscillator strength density is very low and the Balmer lines are completely dissolved (Dappen et al. 1987).

As an example of using the predicted spectra to estimate the electron density in the region of Balmer line formation, we plot in Figure 4 the line profile and contribution function for the Hγ line calculated with the TB09+HM88 profiles in RH. The contribution function indicates where emitted line intensity originates as a function of atmospheric height and wavelength, such that integrating the contribution function over height reproduces the line profile. In the top panel of Figure 4, we plot the contribution function for Hγ at line center (dotted line) and in the far wing (dashed line). The wavelengths where these contribution functions are measured are indicated with corresponding vertical lines in the line profile plot in the bottom panel. The solid line in the top panel shows the electron density measured on the right axis. Together these indicate that the intensity near line center forms in a region with electron density ranges from ∼(3–7) × 10^{12} cm^{-3} and the far wings (λ_c + 20 Å) form in a region with ∼(4–5) × 10^{14} cm^{-3}.

4. Balmer Line Broadening in Stellar Flares

In our previous work (Allred et al. 2005, 2006; Kowalski et al. 2015b, 2016, 2017), we used the RADYN code (Carlsson & Stein 1997) to simulate the dynamics of flaring loops in solar and dMe atmospheres. We refer the reader to Allred et al. (2015) for an extensive description of the RADYN flare code.

The widths of the Balmer lines are often used to compare to models of pressure broadening (Svestka 1963; Švestka & Fritzová-Švestková 1967) to infer an electron density, while the profile shapes in the line wings have been compared to theoretical model predictions (Doyle et al. 1988; Eason et al. 1992; Allred et al. 2006; Paulson et al. 2006). The highest order Balmer lines that are resolved have been used with the Inglis–Teller relation to probe the charge density in flares (Kurochka & Maslennikova 1970; Hawley & Pettersen 1991). To account for self-consistent optical depth, density, and temperature variations over the regions of line formation, we use our modeling method to revisit the broadening predictions from recent RHD flare models of dMe flares that produce large values of the electron density ($n_e \gtrsim 10^{15}$ cm^{-3}). These comparisons can be extended to solar flare model atmospheres that exhibit lower electron density values of $n_e \sim 10^{13}$–5×10^{14} cm^{-3} (Donati-Falchi et al. 1985; Johns-Krull et al. 1997; Kowalski et al. 2017) to make predictions for the Daniel K. Inouye Solar Telescope (DKIST).

4.1. Instantaneous Model Predictions

In Kowalski et al. (2015b) and Kowalski et al. (2016), we presented model flare atmospheres heated by a high flux of nonthermal electrons (10^{13} erg cm^{-2} s^{-1}; F13) which produce a $T \sim 10^4$ K blackbody-like continuum flux distribution as observed in many flares from active M dwarf stars. The hot blackbody-like continuum distribution results from large continuum optical depths from a dense, heated chromospheric condensation. The charge density in the continuum-emitting layers achieves a maximum value of ∼5 × 10^{15} cm^{-3}. The opacity effects from level dissolution produces Balmer continuum flux[15] at wavelengths longer than the Balmer limit (3646 Å) and higher order Balmer emission lines that fade into this continuum flux. These properties have been observed in high-resolution spectra of a large dMe flare (Fuhrmeister et al. 2008). With the S78 approximations as Voigt profiles in the RH code, the highest order Balmer lines that are predicted at this charge density are H10/H11, which is reasonable compared to the observations of some dMe flares (Kowalski et al. 2013, 2016).

Because of the computation time required for the convolution (Equation (1)), it is unfeasible to incorporate the TB09 +HM88 method directly into RADYN. Instead, we input snapshots of the atmospheric state from RADYN into RH. It is well-known that the flaring atmosphere is very dynamic. The dynamics and the proper time-dependent ionization (electron density) at each snapshot are included, but statistical

[15] The Balmer continuum flux from level dissolution is sometimes also referred to as the pseudo-continuum flux, or as the L–Z continuum flux in Kowalski et al. (2015b).

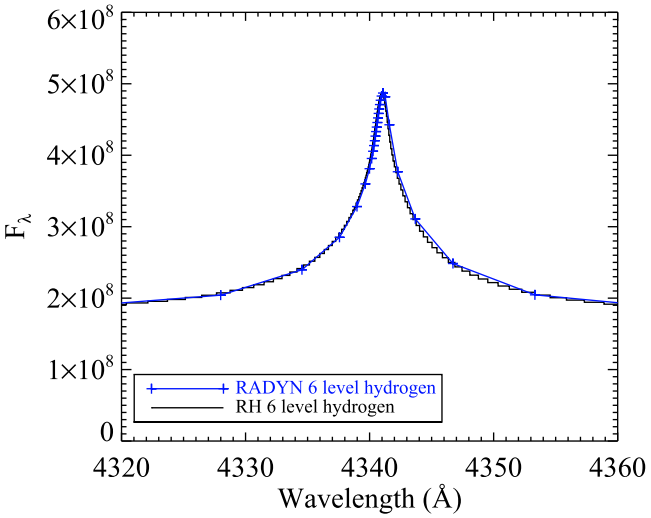

Figure 5. Comparison of the F13 dpl at $t = 2.2$ s Hγ line profile calculated with RADYN (with non-equilibrium ionization and excitation) and RH (with non-equilibrium ionization). The statistical equilibrium assumption for excited levels of hydrogen employed in RH does not have an effect on the line profile (at this time step). In this comparison, both calculations use the S78 prescription for electric pressure broadening.

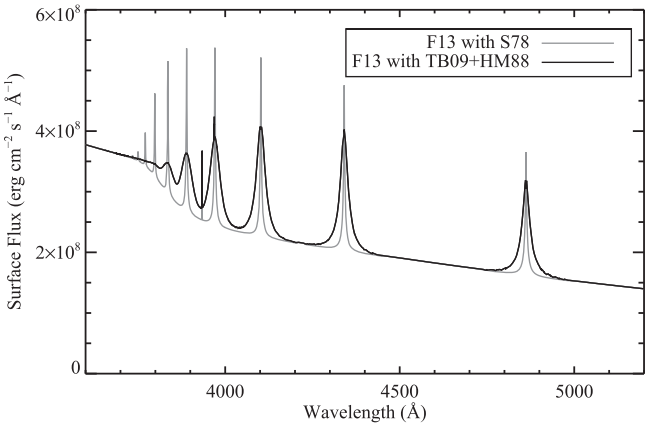

Figure 6. Flare model spectrum (F13 $\delta = 3$ at $t = 2.2$ s) from $\lambda = 3600$–5200 Å calculated with RH with the TB09+HM88 broadening compared to the S78 broadening. The S78 spectrum is obtained from the F13 model in Kowalski et al. (2016) using the method of Kowalski et al. (2015b). The opacity effects from dissolved levels are included in both calculations. Instrumental convolution has not been applied here. The TB09+HM88 profiles produce much broader Balmer lines than S78. In the TB09+HM88 calculation, the higher order Balmer lines fade into the dissolved level continuum flux at a longer wavelength than the S78 prescription.

equilibrium for the excitation is assumed in solving the radiative-transfer equation in the RH calculation. To understand the extent of this limitation, we plot Balmer lines modeled using RADYN and RH in Figure 5. For this comparison, RH has been configured to most closely match the radiative-transfer method in RADYN, (i.e., using a 6-level hydrogen atom, complete redistribution, and S78 broadening). In this configuration, the only difference between the radiative-transfer methods employed by these codes is the assumption of statistical equilibrium in the excited levels employed in RH. Figure 5 indicates that, for the $t = 2.2$ s snapshot in the F13 model from Kowalski et al. (2015b), the statistical equilibrium limitation is a small effect, justifying our use of RH. The same is true for $t = 2.2$ s of the F12 model presented in Kowalski et al. (2015b).

In RH, the occupational probability formalism is not included in the rate equations for statistical equilibrium as described in detail in Hubeny et al. (1994). In our implementation, we include the occupational probability prescription only in the non-LTE bound–bound and bound–free opacity and emissivity (Section 2, see also Kowalski et al. 2015b). Including occupational probabilities in the rate equations for statistical equilibrium in RH would likely affect the electron density and the populations of the upper levels of hydrogen. At this expense, we use the non-equilibrium electron density from a snapshot from RADYN. The agreement with the observed spectrum of Vega (Section 3) justifies that the method currently employed in RH is sufficiently accurate for atmospheres that are near LTE conditions in their continuum-emitting layers, as is the case for the F13 flare models at $t = 2.2$ s (see the discussion in Kowalski et al. 2015b).

We repeat the RH calculation with the TB09+HM88 profiles convolved with the Voigt function for the $\delta = 3$, F13 model atmosphere at $t = 2.2$ s from Kowalski et al. (2016) and for the double-power-law ($\delta = 3$ at $E < 105$ keV, $\delta = 4$ at $E > 105$ keV) F13 model at $t = 2.2$ s (hereafter, F13 "dpl") from Kowalski et al. (2015b). The new prediction in the Balmer jump wavelength region is shown in Figure 6 for the F13 $\delta = 3$ at 2.2 s, which exhibits broader Balmer lines, while H9 is the highest order Balmer line that is not completely transformed into Balmer continuum flux longward of the Balmer edge. With the S78 method, H11 is the bluest detectable (undissolved) Balmer line in emission. We use the TB09+HM88 profiles, which have been calculated with $\beta_{\rm crit}$ but find that these increase the peak of the H8 Balmer line and decrease the trough between H8 and H9 by ∼2% compared to a calculation without $\beta_{\rm crit}$ (VCS, no psuedo-continuum). Using the TB09+HM88 profiles, the H10 and H11 lines are broadened much more than with the S78 prescription (Figure 1); the occupational probability for the upper levels of these transitions are small, which causes the flux at these wavelengths to be dominated by dissolved level continuum flux in the emergent spectrum. Higher order Balmer lines in the impulsive phase that are as faint (relative to the nearby continuum) as the new F13 prediction are very rare (e.g., García-Alvarez et al. 2002).

We convolve the F13 model spectra in Figure 6 with a representative spectral resolution ($R \sim 450$) from the flare spectral atlas of Kowalski et al. (2013) and calculate the width at 10% of maximum line flux (0.1 width) for the Hγ line to be 78 Å for the TB09+HM88 prescription and 32 Å for the S78 prescription. For the F13 dpl at $t = 2.2$ s, the 0.1 width of Hγ is larger, ∼100 Å with the TB09+HM88 broadening. Typical line widths in dMe flares are 15–20 Å for large flares at moderate spectral resolution (Hawley & Pettersen 1991); the maximum observed 0.1 widths for the Hγ line at low spectral resolution are 30–40 Å (Figure 4.13 of Kowalski 2012) at times of brightest line emission, but the line broadening has been observed to be larger (45–50 Å) in the mid-rise phase of large flares (Figure 4.14 of Kowalski 2012). The contribution function-weighted charge density over which the Hγ line forms is $\sim 3.5 - 5 \times 10^{15}$ cm^{-3} for the F13 $\delta = 3$ (and 4–6×10^{15} cm^{-3} for the F13 dpl) at $t = 2.2$ s. The F13 model with TB09+HM88 profiles demonstrates that the F13 instantaneous spectrum at 2.2 s, and therefore this range of charge density, is not consistent with even the largest observed values of the broadening in flares. In Section 4.2, we show that adding

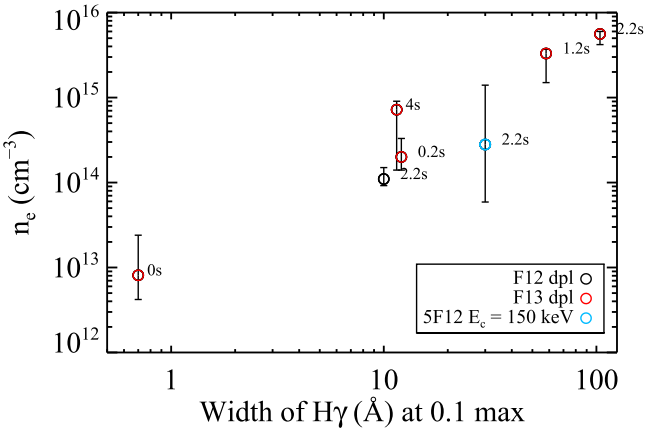

Figure 7. Electron density weighted by the contribution function to the emergent intensity ($\mu = 0.95$) vs. the 0.1 width of the Hγ line (without instrumental convolution). The values are shown for representative times during the F13 dpl flare simulation, for the F12 dpl simulation (at $t = 2.2$ s), for our pre-flare M dwarf model atmosphere, and for a new flare simulation with an energy flux of 5F12, $E_c = 150$ keV, and $\delta = 3$. The circles show the mean electron density over the line, and the upper and lower error bars show the maximum and minimum electron density over the line. The "far wing" values described in the text refer to the value of the contribution function-weighted electron density at $\lambda_{\rm rest} + 20$ Å, which approximately corresponds to the upper error bar. There is a general trend with slope $\approx 2/3$ for the snapshots from the F13 simulation.

flux spectra with lower broadening (at earlier and later times in the heating simulation) to emulate simultaneously heating and cooling loops produces a broadening that is closer to the observations. Because of the larger broadening with the TB09 +HM88 profiles, the emergent line intensity in the F13 model originates from a larger physical depth range in the atmosphere, and the wavelength-integrated emergent line flux of the Balmer lines is therefore also several times (∼2.5×) larger than in the case of the S78 profiles.

In Figure 7, we plot the widths of the Hγ line for the evolution of the F13 dpl simulation compared to the width of the line from the F12 dpl simulation from Kowalski et al. (2015b) in order to bracket the range of electron densities relevant for flares ($10^{13} - 5 \times 10^{15}$ cm^{-3}). For the F13 dpl model evolution in Figure 7, the slope of the relation is approximately $2/3$, which is the expected scaling of the wavelength shift from electric pressure broadening (see, e.g., Johns-Krull et al. 1997):

$$\Delta\lambda \propto n_e^{2/3} \left\{ \frac{n^2}{n^2 - 4} \right\}^2 [n(n-1) + 2]. \quad (2)$$

It is interesting to understand the difference between density estimates using TB09+HM88 and S78 for the $t = 2.2$ s of the F13 $\delta = 3$ simulations in Figure 6. Using the S78 theory gives a 0.1 Hγ width of 16 Å, which is a factor of nearly five lower than with the TB09+HM88 profiles. Using the relation from the TB09+HM88 broadening models in Figure 7, a broadening of 16 Å gives an electron density that is a factor of 5–10 lower than the range in the RHD (RADYN) calculation. The results of Johns-Krull et al. (1997) demonstrated a similar discrepancy between the S78 treatment and the modified impact theory of Kepple & Griem (1968) and Bengtson et al. (1970).

According to Equation (2), the widths of higher order lines should increase significantly (e.g., Hα compared to Hγ), in the regime where thermal broadening is comparatively small. However, the interline optical depth variation results in much less extreme width differences (Svestka 1962, 1963). In our models (and generally in the observations too), the broadening is not strongly dependent on the Balmer transition because the much larger optical depth for Hα near line center leads to a much smaller (∼100×) physical depth range over which the line is produced compared to Hγ, thus giving a larger value of the 0.1 width for Hα than indicated by Equation (2). We also note that directly comparing to the width of the $S(\alpha)$ profiles results in largely erroneous values of the electron density; due to the optical depth over the line, the values of $S(\alpha)$ in the far wings at $S(\alpha) \sim 10^{-4}$ are the important determinant in the 0.1 width of the line when the optical depth near line center and the emissivity in the line wings are both large, as in the Balmer line profiles of Vega.

In Figure 7, the width of Hγ is shown from a new electron beam heating simulation with a flux of 5×10^{12} erg cm^{-2} s^{-1} (5F12) that is calculated with the RADYN flare code, using a high, low-energy cutoff of $E_c = 150$ keV so that the heating occurs deep in the atmosphere (see Appendix A). The emergent continuum spectrum has a small Balmer jump ratio and the low-order Balmer lines are broad and in emission with a prominent central reversal. Like for Vega the Hγ line is formed over a large range of electron densities, given by the error bar range in Figure 7, which demonstrates that a line width value does not always correspond to a unique electron density value; this is also true for the F13 model atmospheres but for a narrower range of electron density. Interestingly, the broadening (75 Å) in the Hγ emission line in the F13 model is comparable to the broadening (nearly 70 Å) in the Hγ absorption line in Vega, while there is an order of magnitude difference in the maximum charge density over the formation heights of the line profile. The Hγ line in the 5F12 $E_c = 150$ keV model forms over an electron density that is comparable to and larger than the electron density that produces the line in Vega, but the broadening is much larger in the Vega spectrum.

The model predictions of the highest order Balmer line in absorption (at least H16) in the Vega spectrum (Figure 3 top) differ significantly from the highest order Balmer line that is in emission (H9) in the F13 spectrum. Therefore, the amount by which the higher order Balmer lines fade into the dissolved level continuum flux at wavelengths longer than the Balmer edge can provide an additional constraint to break such a degeneracy and ambiguity in the charge density-line width relation in flare atmospheres. In the 5F12 model, the highest order Balmer line that is not completely dissolved is ≈H13, and the far wing of Hγ ($\lambda_{\rm rest} + 20$ Å) forms over an electron density that is three times as great as that in Vega (at the same wavelength) but a factor of three lower than the F13 model (at the same wavelength). This ordering by electron density is consistent with the highest order Balmer line in each model spectrum. Kowalski et al. (2015b) discussed a dissolved line decrement[16] using H11/Hγ that can be used to quantify the degree by which the higher order lines fade into continuum flux; we intend to pursue this diagnostic in a future work with NLTE flare models and the TB09+HM88 broadening.

4.2. The Balmer Line Broadening from Many Flare "Threads"

F13 beam flux model atmospheres produce dense, downward-directed, heated compressions ("chromospheric condensations")

[16] Referred to as an "L–Z decrement" in Kowalski et al. (2015b).

and have been found to adequately explain the hot (10^4) blackbody-like, optical and NUV continuum flux distribution of flares on active M dwarf stars (Kowalski et al. 2015b, 2016). However, the new broadening predictions show that these white-light emitting compressions result in a charge density ($\sim 5 \times 10^{15}$ cm^{-3}) that over-broadens the Balmer lines as in Figure 6 compared to observations in the literature. If such dense compressions are formed in dMe flares, then they would have to account for a large fraction of the continuum flux and a small fraction of the line flux, such that the spatially integrated flare spectrum exhibits narrower lines than the TB09+HM88, F13 $t = 2.2$ s prediction.

Kowalski et al. (2015b) used a time-average of the F13 model atmosphere over its evolution to more realistically simulate the prediction over an exposure time. Averaging over the F13 simulation is equivalent to an instantaneous measurement of a spatially unresolved observation of many F13 flare loops sequentially being initiated at regular, short time intervals corresponding to different locations on the star. This prescription for representing the flare flux from many flare "threads," or kernels, is similar to the "multithread" modeling that has been successful in reproducing spatially unresolved solar flare light curves in *GOES* soft X-rays Warren (2006). A method for multithread modeling with RADYN heating models lasting ~15–20 s was further developed in Rubio da Costa et al. (2016) and has also been employed in Reep et al. (2016). In multithread modeling of solar flares, the flux of each thread changes over the evolution of the flare (Warren 2006) such that impulsive phase threads have a higher flux than gradual phase threads. For simplicity, we use the F13 model to represent all heated threads (kernels).

We simulate a multithread prediction for the line broadening from the F13 simulations in Kowalski et al. (2015b) and Kowalski et al. (2016). We use the snapshots from Figure 7 at $t = 0.2$, 1.2, 2.2, and 4.0 s (the electron beam heating is turned off at 2.3 s and allowed to relax until $t = 5$ s) to sample the range of atmospheric conditions and brightness values achieved in the models. The assumption of statistical equilibrium (without the occupational probability formalism of Hubeny et al. 1994) was justified in Sections 3 and 4.1 but may not be appropriate within the earliest tenths of seconds after the beam heating starts. The Balmer lines are broadest at $t = 2.2$ s when the chromospheric condensation has achieved the maximum electron density at $T \sim$ 12,000–13,000 K, thus averaging over earlier and later times decreases the line broadening in the multithread models. For the F13 dpl multithread (0–5 s average) model, the 0.1 width of Hγ is ~50 Å, a factor of two narrower than at $t = 2.2$ s; for the F13 $\delta = 3$ multithread (0–5 s average) model, the 0.1 width is 40 Å (compared to 75 Å at 2.2 s; Figure 6). The 0.1 width of the F13 $\delta = 3$ is near the upper range of observed values in the early impulsive phase but are still quite high. Whereas the S78 predictions from the F13 model at 2.2 s for the continuum flux ratios[17] (C3615/C4170, C4170/C6010), the line-to-continuum ratio values of Hγ/C4170 (=10–20), and broadening are generally consistent with peak phase spectra of dMe flares (Kowalski et al. 2015b, 2016), the time-averaged values with TB09+HM88 broadening are more consistent with the early impulsive rise phase of some dMe flares in the literature, as concluded in Kowalski et al. (2015b) for the time-average continuum properties of the F13 dpl model. For example, the time-resolved impulsive phase data of the large IF3 flare event from Kowalski et al. (2013) exhibit values of (C3615/C4170, C4170/C6010, Hγ/C4170, 0.1 width Hγ) = (2.2, 1.8, 40, 48 Å) in the early-to-mid rise phase (S#27, cf Figure 30 of Kowalski et al. (2013)) that are very similar to these quantities (2.1, 1.8, 45, 45 Å, respectively) from the F13 $\delta = 3$ multithread model (Table 1).

[17] For example, C3615/C4170 is the ratio of the continuum flux averaged in the 30 Å window around $\lambda = 3615$ Å to the continuum flux averaged in a 30 Å window around $\lambda = 4170$ Å.

4.3. Balmer Decrements

Balmer decrements are defined as the ratio of the excess (i.e., background subtracted) flux in Balmer lines to that of the Hγ line and are also used to constrain the charge density variations in flares (Hawley & Pettersen 1991; Jevremovic et al. 1998; García-Alvarez et al. 2002). The observed decrements in dMe flares are typically Hβ/H $\gamma \sim$ 1.0–1.2 and for Hδ/H $\gamma \sim$ 0.75–1.05 (Table 4.20 of Kowalski (2012), Table 1 of Allred et al. 2006). Decrements are similarly used in solar flare studies as well, but the lack of broad wavelength coverage spectra make the measurements rare in the modern era (Johns-Krull et al. 1997; Kowalski et al. 2015a). Since Balmer decrements have been widely used, it is informative to study how they may vary in response to electric pressure broadening with the new TB09+HM88 profiles.

In Table 1, we show the decrements for the two F13 models at $t = 2.2$ s and the 0–5 s average (multithread) model (Section 4.2) calculated with the TB09+HM88 broadening. Although the line flux increases by ~2.5× with TB09+HM88 compared to the line flux calculated with the S78 broadening, the line flux ratios do not change appreciably between the two methods. The Hβ/Hγ and Hα/Hγ line flux ratios are much smaller in the models than typical values from observations, but the Hδ/Hγ ratios are in general agreement. Such small values of Hα and Hβ to Hγ indicate a "reverse decrement" and are only observed to be as low as ~0.8 (for Hα; Figure 4.22 of Kowalski 2012). The Hα/Hγ line flux ratios are very low in the F13 models because the optical depth necessary to produce the hot blackbody-like continuum shape results in a very large Hα optical depth and radiation thus escapes from a much smaller physical depth range of the atmosphere across this line compared to Hγ. We have also computed the line flux ratio at $t = 0$ s in our M dwarf model (row 1), which is in good agreement with observations (Bochanski et al. 2007, see also Table 2.8 of Kowalski et al. 2013) but with a significantly larger line flux ratio for Hβ and slightly larger ratio for Hα than in the observations. The discrepancy could result from the difference between spatially resolved and averaged observations, and 3D effects (Walkowicz 2008; Uitenbroek & Criscuoli 2011; Leenaarts et al. 2012; Wedemeyer & Ludwig 2015). As in the flare simulations, the Hδ/Hγ line flux ratio is consistent with the observations.

It is interesting to compare the values in Table 1 to the method of Drake & Ulrich (1980), which presented the Balmer line decrements for a large parameter space of electron density, temperature, and optical depth for a homogeneous slab of hydrogen. In addition, approximations were made using the escape probability from the line wing and the optical depth variation from line to line. In their Appendix B, they present the decrements for $n_e = 10^{15}$ cm^{-3}, which is the highest density that they considered: the Hα/Hγ, Hβ/Hγ, and Hδ/Hγ decrements are 1.8, 1.2, and 0.85, respectively. The values for their limiting optically thick case, on the other hand, show

Table 1
Balmer Decrements and Hγ Broadening with TB09+HM88

Model	Hα	Hβ	Hγ	Hδ	0.1 width Hγ (Å)	Hγ/C4170	C3615/C4170	C4170/C6010
pre-flare[a]	5.9	2.7	1.0	0.58	...	...	...	...
F13 2.2s dpl	0.3	0.7	1.0	0.8	100 (100)	45	1.8	2.1
F13 dpl multithread (0–5 s ave)	0.4	0.8	1.0	0.9	52 (60)	74	2.6	1.6
F13 2.2s $\delta = 3$	0.3	0.8	1.0	0.9	75 (78)	31	1.7	2.3
F13 $\delta = 3$ multithread (0–5 s ave)	0.4	0.9	1.0	1.0	40 (45)	45	2.1	1.8

Note.
[a] The pre-flare atmosphere is the most up-to-date version of the pre-flare state in our modeling, which is described in Appendix A. The continuum flux ratios C3615/C4170 and C4170/C6010, and the line-to-continuum flux ratio (Hγ/C4170) are also given. The values in parentheses for the Hγ widths are calculated with an instrumental convolution of $R = 450$.

reverse decrements for Hα and Hβ but are not as extreme as for the F13 model at $t = 2.2$ s, likely due to the factor of five larger electron density in the F13 model. The results from Drake & Ulrich (1980) are qualitatively similar to ours for flare atmospheres that are so dense that they are approximately homogeneous in electron density (e.g., at $t = 2.2$ s of the F13 dpl model, the contribution function-weighted electron density varies from only (4–6) $\times 10^{15}$ cm^{-3} over the Hγ line), but would not be applicable to the flare atmospheres that exhibit a large range of electron density over the line formation, such as the high, low-energy cutoff (5F12, $E_c = 150$ keV) flare model in Figure 7 with a range of nearly a hundred in electron density.

5. The Line Broadening and Flux Decrements in the YZ CMi Megaflare

In this section, we model the Balmer decrements and broadening during the Megaflare on the dM4.5e star YZ CMi (Kowalski et al. 2010), which has high-time resolution, flux-calibrated NUV, and optical spectra. The U-band light curve from Kowalski et al. (2010) is shown in Figure 8. The Megaflare ($E_U > 10^{34}$ erg) consisted of a series of high-energy ($E_U \sim 10^{32}$ erg) secondary flares after the big first flare (BFF) event at $t = 0.45$ hr in Figure 8.

During the rise and peak of the secondary flare MDSF2 in the decay phase of the Megaflare, a blackbody fit to the blue continuum ($\lambda = 4000$–4800 Å) indicates an increasing color temperature while the line fluxes decrease for the (quiescent-subtracted) flare spectrum. Subtracting the decay phase spectrum just before the start of MDSF2 reveals the spectrum similar to an A star (Section 6.3 and Figure 25 of Kowalski et al. 2013); the veiling from this spectrum causes the Balmer flux decrement of the total flare flux to tend toward an A0-star decrement and the 0.1 widths of the emission lines in the total flare spectrum to decrease below the resolution limit (13 Å). This flare flux component has been modeled as a phenomenological hot spot with $T_{\rm max} = 20{,}000$ K in the photosphere (Kowalski et al. 2011). We have successfully reproduced a similar spectrum with the RADYN code using a very high, low-energy cutoff of the electron beam, $E_c = 500$ keV, a moderately large flux of 2×10^{12} erg cm^{-2} s^{-1}, and a very soft spectrum, $\delta = 7$. Accurate treatment of the energy loss from this electron beam requires the fully relativistic Fokker-Planck solution that is currently employed in the RADYN flare code (Allred et al. 2015).[18] As in the F13 models, the electron beam energy flux at the top of the atmosphere is kept constant for

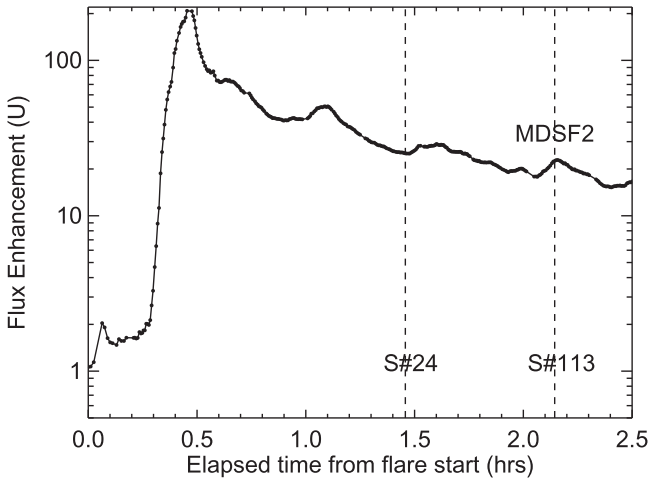

Figure 8. U-band light curve of the YZ CMi Megaflare event. The times of the gradual decay phase spectrum (S#24) and the peak spectrum (S#113) of the secondary flare MDSF2 are indicated. Note that several secondary flares also occurred before S#24.

2.3 s and the atmosphere is allowed to relax after 2.3 s. Shocks do not develop in this model, and the atmosphere can relax to much longer times than the F13, and the simulation takes much less computation time. We use the RH code with the TB09+HM88 profiles for Balmer line broadening and level dissolution and calculate the emergent flux spectrum at $t = 2.2$ s. The model spectrum is shown as the pink spectrum in Figure 9.

The Balmer lines and Balmer continuum are in absorption in the emergent flux spectrum, similar to the A0 star Vega; we thus use this beam-heated atmosphere to represent the newly formed flux during the secondary flare MDSF2. The properties of this model atmosphere are discussed in Appendix A. In summary, a temperature maximum peaking at nearly $T \sim 13{,}000$ K is formed in the very low chromosphere where the temperature is 4000 K before the flare heating starts. We interpret the deep heating in this model as a "hotspot" as in the static, phenomenological model of Kowalski et al. (2011). With the new RHD model, we have deduced that the hot spot can form much higher ($\log m/{\rm g\ cm^{-2}} = -2.05$ to -1.25) than in the phenomenological static model ($\log m/{\rm g\ cm^{-2}} = 0.5$).

We compare the new RHD models with new (TB09+HM88) broadening to spectral observations of the flare-only (quiescent-subtracted) flux at two times in the YZ CMi Megaflare: spectrum S#24 consisting mostly of decay phase flux at the tail end of a secondary flare and spectrum S#113 at the peak of the secondary flare MDSF2. The times of S#24, S#113, and

[18] Whereas the F13 models here were calculated with the non-relativistic prescription in Emslie (1978).

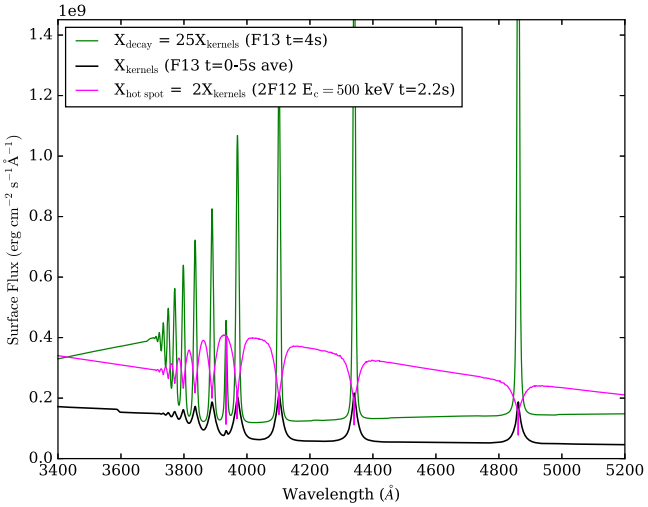

Figure 9. Surface flux spectra for each of the components ($F_{\rm decay}$, $F_{\rm kernels}$, $F_{\rm hotspot}$) multiplied by the respective filling factor, X. The models are superposed with these filling factors to produce the model spectra in Figure 10. The relative filling factors are indicated by the values of X in the legend. In Figure 10 (top), $X_{\rm kernels} = 0.0009$ and in Figure 10 (bottom panel), $X_{\rm kernels} = 0.00047$. These spectra were calculated with RH and the TB09 +HM88 profiles.

MDSF2 are indicated in Figure 8. The observed properties of the YZ CMi Megaflare are presented in Kowalski et al. (2013) and are summarized in Table 2 (rows 1–2) for S#24 and S#113. We also include continuum flux ratios (C3615/C4170 and C4170/C6010) here to compare to the model predictions of the continuum shape. Following Hawley et al. (2003) and Osten et al. (2016), we model the flare-only flux observed at Earth as

$$F_{\rm flare\text{-}only,Earth} = [F_{\rm kernels}X_{\rm kernels} + F_{\rm decay}X_{\rm decay} + F_{\rm hotspot}X_{\rm hotspot}]\frac{R_{\rm star}^2}{d^2} \quad (3)$$

where d is the distance to YZ CMi and $R_{\rm star} = 0.3R_{\rm Sun}$, F is a surface flux spectrum of a model component and X is the filling factor, which is the fractional area of the visible stellar hemisphere that is emitting at each value of F (Hawley et al. 2003). The three model component spectra ($F_{\rm kernels}$, $F_{\rm decay}$, $F_{\rm hotspot}$) superposed to produce the model flare-only[19] flux at Earth are shown in Figure 9. $F_{\rm kernels}$ is the F13 dpl multithread model (0–5 s average; Table 1), $F_{\rm decay}$ is the F13 dpl model at $t = 4$ s, and $F_{\rm hotspot}$ is the 2F12 $E_c = 500$ keV model at $t = 2.2$ s. Each flux component has been calculated using RH with the TB09+HM88 profiles. The phenomenology of "kernels," "decay," and "hotspot" is discussed in Section 5.1.

Following the analysis of the DG CVn superflare presented in Osten et al. (2016), we assume $X_{\rm decay} = 25X_{\rm kernels}$ and $X_{\rm hotspot} = 0$ for S#24 and solve for $X_{\rm kernels}$ using the flare-only, specific continuum flux centered at $\lambda = 4170$ Å and $\lambda = 4785$ Å observed at Earth. For S#113, we assume $X_{\rm decay} = 25X_{\rm kernels}$ and find that $X_{\rm hotspot} = 2X_{\rm kernels}$ by fitting to the Balmer jump ratio (C3615/C4170 = 1.5) in the observation; then we solve for $X_{\rm kernels}$ using the flare-only, specific continuum flux centered at $\lambda = 4170$ Å and $\lambda = 4785$ Å observed at Earth. The value of $X_{\rm kernels}$ is 0.0009 for S#24 and 0.00047 for S#113. We refer to the model for S#24 as "the DG CVn Superflare F13 multithread model" and the model for S#113 as "the DG CVn Superflare F13 multithread model + Hot Spot."

The results of the model comparison to the observation of S#24 are shown in the top panel of Figure 10; the Balmer line flux decrements and broadening, and continuum flux ratios of the model are shown in the third row of Table 2. We find that the DG CVn Superflare F13 multithread model improves the model broadening and decrements of the Balmer lines that were found in Section 4.2. The widths and flux decrements are in striking agreement with the decay phase spectrum (S#24) of the Megaflare, as are the continuum flux ratios. From Table 1 it is clear that neither the F13 multithread model (0–5 s average) nor the instantaneous F13 model at $t = 2.2$ s alone account for the continuum and line properties in the YZ CMi Megaflare decay phase (S#24); an additional filling factor of the instantaneous F13 model prediction at $t = 4$ s is necessary to decrease the broadening and increase the Hβ/Hγ decrement in the flare-only model spectrum. The continuum flux ratio C4170/C6010 also becomes lower, in agreement with the observations. The Hγ/C4170 value is higher than in the observations but still in general agreement. Apparently, the same two-component multithread model in the decay phase of an $E \sim 10^{36}$ erg secondary flare event (F2; Osten et al. 2016) during the DG CVn Superflare can also adequately explain the Balmer line and continuum flux properties in the decay phase (S#24) of the secondary flare events (e.g., at $t = 1.1$ hr in Figure 8) in the YZ CMi Megaflare. For a comparison of the continuum flux properties in the DG CVn Superflare and in the YZ CMi Megaflare, we refer the reader to Osten et al. (2016).

For S#113, we use the 2F12 $E_c = 500$ keV (hotspot) model to represent the newly formed flare emission at the peak of the secondary flare MDSF2 and add this model component to the two-component DG CVn Superflare multithread model (Equation (3)). The resulting line and continuum properties for the superposed flare flux model are shown in the last row of Table 2, and the model spectrum and the observation of S#113 are shown in the bottom panel of Figure 10. The superposition of the 2F12 $E_c = 500$ keV (hotspot) model with the DG CVn Superflare multithread model explains several observed changes in the flare-only spectra from S#24 (top panel of Figure 10) to S#113 (bottom panel of Figure 10). The model Hβ/Hγ ratio increases and the Hδ/Hγ ratio decreases, as observed. The line width of Hγ decreases due to the superposition of the broad absorption wings from the high, low-energy cutoff model ($E_c = 500$ keV) and the emission lines from the DG CVn Superflare F13 multithread model; the Hγ/C4170 ratio decreases from 120 to 30, qualitatively similar to how the observations decrease from 90 to 40, and the red continuum (C4170/C6010) becomes bluer (hotter) as in the observations. The Hα line was saturated for these spectra, but we give the model values to show that the values of 0.8–1.0 are consistent with observed values of the reverse decrement in other flares.

In the models in Figure 10, the opacity effects from level dissolution are also included, showing that the spectral properties at $\lambda = 3646$–3800 Å are adequately reproduced by the merging of the Balmer line wings and the continuum flux

[19] The precise comparison of the model predictions to the observed flare-only flux requires subtracting the pre-flare surface flux spectrum scaled by the filling factor of each flare surface flux component (Equation (3) of Kowalski et al. 2016); here, the flare surface flux spectra are much greater than the pre-flare surface flux spectrum and thus Equation (3) is a sufficient comparison to the observed flare-only flux.

Table 2
Comparison to the YZ CMi Megaflare

Observation (S#)	Hα/Hγ	Hβ/Hγ	Hδ/Hγ	Hγ 0.1 width (Å)	Hγ/C4170	C3615/C4170	C4170/C6010
decay phase observation[a] (S#24)	···	1.26	0.86	14.6	87 ± 11	2.7	1.1
secondary flare observation[a] (S#113; MDSF2)	···	1.50	0.75	12.6	42 ± 2	1.5	1.6
Model							
DG CVn Superflare F13 multithread model[b]	0.83	1.18	0.8	14.4 (21)	120	2.9	1.0
DG CVn Superflare F13 multithread model + hot spot[b]	1.0	1.3	0.7	12.6 (18)	30	1.5	1.7

Notes.
[a] These spectra include the flare-only flux with the quiescent spectrum subtracted (see Kowalski et al. 2013). S#24 is shown in Figure 10 (top) and S#113 is shown in Figure 10 (bottom).
[b] "The DG CVn Superflare F13 multithread model" is the F13 dpl model averaged over 0–5 s with a filling factor of $X_{\rm kernels} = 0.0009$ added to the F13 dpl model at $t = 4$ s with a filling factor of $25X_{\rm kernels}$; this model is shown in the top panel of Figure 10. The "DG CVn Superflare F13 multithread model + hot spot" is the F13 dpl model averaged over 0–5 s with a filling factor of $X_{\rm kernels} = 0.00047$ added to the F13 dpl model at $t = 4$ s with a filling factor of $25X_{\rm kernels}$ plus the spectrum at $t = 2.2$ s from the 2F12 $E_c = 500$ keV simulation with a filling factor of $2X_{\rm kernels}$; this total model spectrum is shown in the bottom panel of Figure 10. The 0.1 width values in parentheses were calculated with a Gaussian instrumental convolution with $R = 670$ as in the observations in Figure 10.

longward of the Balmer edge.[20] To match the models precisely to the observations, more flux and less broadening in the Balmer lines and more flux in the Ca II K line are needed in the models without largely affecting the continuum flux distribution (the Hγ/C4170 in the model for S#24 is higher than the observations, but appears lower in flux because of the slightly larger broadening). Additionally, a smaller amount of level dissolution for the higher order Balmer lines is required in the total model spectra of the flare-only flux. In Section 6.1, we speculate on future modeling improvements to explain these discrepancies.

5.1. Interpretation: Extending the Solar Flare Analogy to Megaflares

Following Kowalski et al. (2012), we interpret the surface flux spectra components (Figure 9) in the S#24 and S#113 spectral observations of the YZ CMi Megaflare using analogous phenomenology from high spatial resolution data of two-ribbon solar flares.

1. $F_{kernels}$: The F13 multithread model spectrum (0–5 s average of the F13 dpl model) represents the spreading ribbons of the Megaflare. As the ribbons spread, new flare loops form, and their initiation is staggered in time so that the spatially integrated flux from this area is equivalent to the 0–5 s time-average of the F13. The area decreases over time ($X_{\rm kernels}$ decrease from 0.0009 at the time of S#24 to 0.0005 at the time of S#113); the beam flux probably also decreases over the gradual phase (Warren 2006) as lower field strengths reconnect higher in the corona. We note that newly heated flare loops are necessary to explain the temporally extended gradual phase of the soft X-ray flux in spatially unresolved *GOES* light curves of solar flares (Warren 2006).

   The spreading ribbons may correspond to the regions that produce the end of the large secondary flare (e.g., at $t = 0.6$ hr or $t = 1.1$ hr in Figure 8, before S#24) that peaked prior to the spectral observations, and/or they may be the continuation of the spreading ribbons from the BFF event with $\Delta U = -5.8$ mag at $t = 0.45$ hr in Figure 8. Recent high spatial resolution images in the Hα red wing (+0.8 Å) with the New Solar Telescope have shown that spreading Hα ribbons are composed of many fine-scale kernels with a size of ∼100 km (Sharykin & Kosovichev 2014; Jing et al. 2016); these kernels are located at the leading edge (Isobe et al. 2007) of the ribbons and are often associated with red-wing asymmetries in Hα. Other chromospheric flare lines, such as Mg II and Fe II, also exhibit red-wing asymmetries. Kowalski et al. (2017) reproduces the general properties of the red-wing asymmetries in Fe II lines in the brightest flare footpoints constituting the two flare ribbons that spread apart in the impulsive phase of the 2014 March 29 X1 solar flare. The RHD model that produces dense, heated chromospheric compressions that are consistent with the spectral observations employed a relatively high electron beam flux (5F11). The F13 model evolution consists of a dense, heated chromospheric condensation but with higher temperature, density, and continuum optical depth compared to the chromospheric condensation properties in the 5F11 model for solar flares (see Appendix C of Kowalski et al. 2017). Thus, the kernels of the spreading ribbons may consist of many ≈F13 beams in dMe flares and lower fluxes, ≈5F11 beams, in solar flares.
2. F_{decay}: We use the F13 $t = 4$ s flux to represent the wake of the spreading flare ribbons $F_{\rm kernels}$, resulting in long-lasting (temporally extended) decay phase flux in the Megaflare that persists for hours and is present through the spectral observations S#24 and S#113. Note that the F13 multithread model (0–5 s average) also consists of this decay phase snapshot ($t = 4$ s), but its contribution in the 0–5 s average represents the rapid decay phase of a kernel. The gradually decaying flux may be analogous to temporally extended decay flux in the "wake" of separating ribbons in solar flares, such as that observed after the peak of the NUV (λ2826) continuum-emitting kernels in the 2014 March 29 X1 solar flare (Heinzel & Kleint 2014; Kowalski et al. 2017) and the temporally extended gradual phase component of optical flare kernels on the Sun (Kawate et al. 2016). We assume that the first large event in the Megaflare (or any of the secondary large events peaking before S#24) produces a wake of persistent, decaying flux behind the spreading ribbons. In our modeling, this flux component is not

[20] Note that the feature near 3704 Å in the observation is a He I line that is blended with the H15 and H16 Balmer lines.

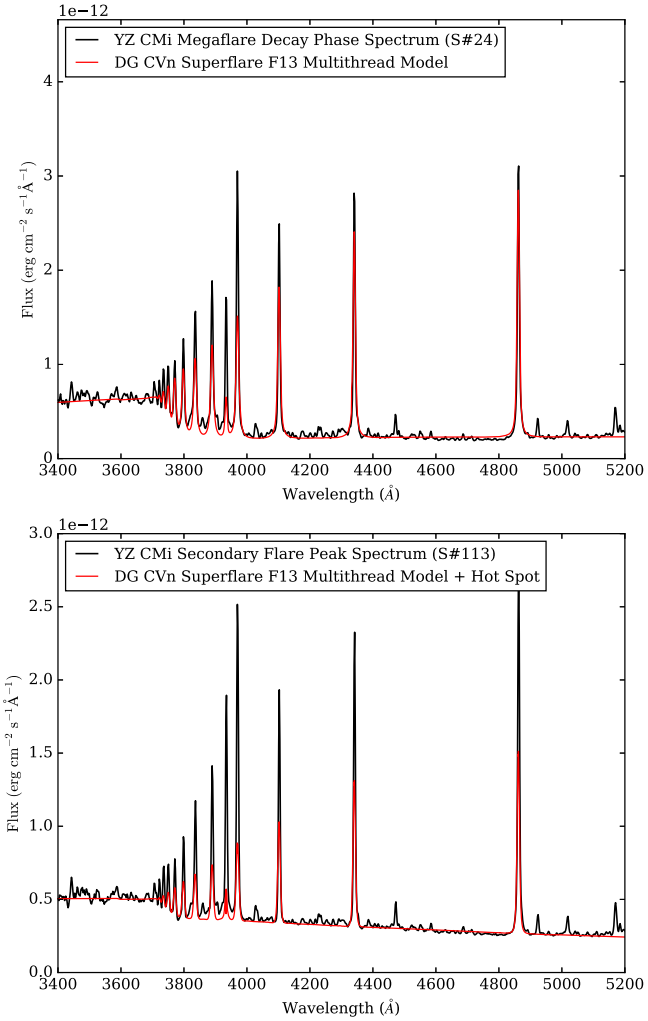

Figure 10. (Top) Model (red) of the flare-only flux for the spectral observation S#24 (black) in the decay phase of the YZ CMi Megaflare. The observed and model quantities are summarized in rows 1 and 3 of Table 2, respectively. (Bottom) Model (red) of the flare-only flux for the spectral observation S#113 (black) of the spectrum at the peak of the secondary flare MDSF2 in the YZ CMi Megaflare. The observed and model quantities are summarized in rows 2 and 4 of Table 2, respectively. The model spectra have been convolved with a Gaussian with FWHM = 6 Å for direct comparison to the observations. The changes in the observed continuum shape and line broadening and fluxes are qualitatively reproduced by the models and are in general quantitative agreement; however, more model flux is needed in the high-order Balmer lines and Ca II while the Balmer lines are slightly overbroadened. The component model surface flux spectra are shown in Figure 9.

self-consistent in the timing relative to one of these peaks in the Megaflare; the NUV continuum exponential decay constant after $t = 2.3$ s in the F13 model is $\tau \sim 0.6$ s, meaning that the pre-flare continuum level would be reached several seconds after the beam heating ends (the F13 models are very computationally demanding, preventing us from currently following the evolution for hours after the beam heating). In Section 5, we found that this flux component is necessary in order to lower the Balmer line decrements and broadening in the model to the observed range of values in S#24. In Section 7, we speculate on directions of future work to better model and constrain the origin of the temporally extended decaying flux component.

We use the high spatial resolution data in the Hα red wing from the DST/IBIS presented in Kowalski et al. (2015a) to estimate the ratio of newly formed kernel area in the spreading flare ribbons to the the area of the intensity in the wake of the ribbons. The IBIS data have a cadence of 20 s and covered several peaks in the X-ray impulsive phase of a two-ribbon, long-duration C1 solar flare, SOL2011-08-18T15:15. For each frame, we measure the area of bright flare intensity that is not bright in the previous frame. We only consider the umbral ribbon, which spreads very slowly across the umbra; most of the apparent kernel motion is parallel along the ribbon. The area of the newly formed Hα kernels is only a small fraction (0.1–0.2) of the total Hα kernel area emitting above the threshold count rate. Thus, it is reasonable to assume that the decay flux ("ribbon wake"; F13 $t = 4$ s) and the newly heated kernels (F13 $t = 0$–5 s average) could reasonably exist in the areal ratio that we employ (1/25) for the DG CVn Superflare and the YZ CMi Megaflare events.

3. $F_{hotspots} = F_{new\ ribbons}$: During the rise and peak of the secondary flare MDSF2, new flare ribbons consisting of new kernels develop. From our RHD modeling of the new flare flux in the secondary flare with the 2×10^{12} erg cm^{-2} s^{-1} $E_c = 500$ keV beam (Appendix A), we infer that the heating scenario in the secondary flare is strikingly different than the heating in the F13 models with $E_c = 37$ keV, where the electron beams lose their energy in the upper chromosphere. In our terminology, hotspots form in the lower chromosphere, which is necessary to produce the Vega-like flare spectrum, and kernels produce chromospheric condensations in the upper chromosphere. $F_{\rm newribbons}$ may produce F13-type heating in addition to hotspot heating. In MDSF2, we infer that the dominant heating goes into forming the hotspot. The filling factor of the hotspot, $X_{\rm hotspot}$, is 0.001, which is remarkably similar to the filling factor inferred from a blackbody fit to the blue continuum with $T = 10{,}000$ K (Kowalski et al. 2010). The filling factor of $F_{\rm decay}$ is 12.5× greater than this, which was also inferred in Kowalski et al. (2010) by fitting an optically thin Balmer continuum (Allred et al. 2006) to the flux at $\lambda < 3646$ Å to represent the decaying Hα ribbons from the main peak. In the three-component phenomenological model of Kowalski et al. (2012), the $F_{\rm kernels}$ component was modeled as a second (cooler) hotspot in the photosphere.

In the superflare from DG CVn (Osten et al. 2016), $F_{\rm kernels}$ was used to represent the newly heated loops after the peak of the high-energy secondary flare event (referred to as F2). The energetic secondary flare F2 had an impulsive phase timescale that was much longer than the "big first flare" event of comparable energy an hour earlier. Thus, different heating scenarios may dominate through the BFF and F2 events in the DG CVn Superflare. A significant detection of continuum flux with a cool color temperature was obtained from the UVW2/V-band and V-band/R-band flux ratios, but the only simultaneous observations to constrain this component occurred after the peak of the F2 event. The continuum flux ratios were adequately explained by the F13 multithread model with decay phase flux without a hotspot contribution, which is the same scenario for the model for the decay phase spectrum S#24 from the Megaflare. When significant time has passed after the peaks of energetic secondary flares, $X_{\rm hotspot} \sim 0$, such

as for the YZ CMi Megaflare at the time of S#24 and for the DG CVn Superflare F2 event at $\approx T0 + 11750$ s and ≈T0+17,000 s (Osten et al. 2016). In future work, we will constrain $X_{\rm hotspot}(t)$ using a superposition of sequentially heated hotspot spectra, as done to produce the F13 multithread model.

In solar flares, there is also evidence that the characteristics of the beam heating can significantly change between the main flare peak and secondary flares. Warmuth et al. (2009) describe a secondary flare that produced a hard X-ray spectrum that could be explained by an electron beam with a higher, low-energy cutoff ($E_c \sim 110$ keV) than in the initial impulsive phase. The parameters of the electron beam for this flare are less extreme but qualitatively similar to the parameters for the $E_c = 500$ keV electron beam that we use to produce a hotspot spectrum. Our modeling of the hotspot implies that the heating may result from ultrarelativistic electrons. Synchrotron emission from ultrarelativistic ($E > 500$ keV) electrons are a possible source for the sub-mm/THz radiation in solar flares (see the review in Krucker et al. 2013). Sub-THz radiation attributed to synchrotron emission has also been detected from stellar flares in active binary systems (Massi et al. 2006).

In Figures 11(b)–(e), we show representative images from the Atmospheric Imaging Assembly (AIA; Lemen et al. 2012) on the *Solar Dynamics Observatory* (*SDO*) in the 1700 filter during the *GOES* X5.4 and X1.3 solar flares of 2012 March 7. The AIA 1700 filter shows the footpoint features (ribbons and kernels) in solar flares at high spatial resolution. There are no simultaneous spectral observations over the wavelength range of this filter, but studies of other solar flares indicate a combination of continuum, line intensity and pseudo-continuum intensity from blended lines (Cook & Brueckner 1979; Doyle & Cook 1992; Brekke et al. 1996; Qiu et al. 2013). The FUV continuum becomes bright in stellar flares (Hawley & Pettersen 1991), and it may be a good tracer of the formation of hot spots in secondary flares (Ayres 2015). The solar flare event of 2012 March 7 provides a unique comparison to the Megaflare because it produced two significant flares in the 1700 light curve (Figure 11(a)), analogous to a "big first flare" and a high-energy secondary flare, within the same active region. Notably, the thermal response detected by *GOES* shows a significant difference compared to the secondary flare in Warmuth et al. (2009), which does not respond in *GOES*, suggesting that the heating mechanism is not uniform among secondary flare events.

In Figures 11(b)–(e), we use the spatial development in the 2012 March 7th solar flare to illustrate possible analogous development of the three continuum-emitting components ($F_{\rm kernels}$, $F_{\rm decay}$, $F_{\rm hotspot}$) in the YZ CMi Megaflare. Combining the spatial development in Figure 11 with the RHD modeling of the Megaflare decay phase spectra, a possible scenario for the spatial development of the Megaflare decay phase is as follows: (1) at the start of the spectral observations, bright kernels with a filling factor of 0.1% are heated by high-flux electron beams at the leading edges of the spreading ribbons (panel d); (2) each kernel rapidly decreases in brightness as beam heating ends. The total flare area that has been swept out by these kernels and other ribbons earlier in the flare has a filling factor of ∼1%–2.5% and decays in brightness on a longer timescale than the rapid brightness decay of each kernel (panel d); (3) later, the total area of the kernels at the leading edges of the separating flare ribbons has decreased in size to a filling factor of 0.05%. These kernels propagate into the locations of the active region where new ribbons with hotspots heated by ultrarelativistic electron beams are triggered and develop with a filling factor of 0.1% (panel e). Also at this time, the locations of the kernels formed in panel (d) are still decaying on a long timescale.

6. Discussion and Future Work

The TB09+HM88 broadening prescription presents a challenge for explaining the white-light continuum flux distribution in dMe flares using high-flux (F13) nonthermal electron beams that generate very dense chromospheric compressions and much broader lines than observed. A multithread modeling approach with the new line broadening gives a more direct comparison to spatially averaged observations of stellar flares, which are a spatial superposition of many flare loops at different stages in their heating and cooling evolution. The multithread modeling shows that the average broadening over the time-evolution of the F13 model is ∼2× lower than the instantaneous maximum broadening, but the Hα and Hβ line flux ratios (relative to Hγ) are too small compared to the observations, though the Hδ decrements are in agreement. The F13 multithread models are consistent with the observed continuum flux ratios, line-to-continuum flux ratios, line broadening, and Hδ/Hγ flux ratio of the early impulsive rise phase but not the main peak of impulsive-type dMe flare events (Kowalski et al. 2013, 2015b).

We applied a multithread model with several flux components and the TB09+HM88 broadening prescription to the phenomenological model of Kowalski et al. (2012) for a representative YZ CMi Megaflare decay phase spectrum. The observed gradual phase spectrum is a superposition of flux components spanning a large range of electron densities and hydrogen Balmer line broadening. Using the multithread modeling with several flux components that was used to explain the white-light continuum properties in the gradual phase of the DG CVn Superflare in Osten et al. (2016), we find that the Balmer decrements, broadening, and continuum flux ratios are well-reproduced in the decay phase spectra of the Megaflare. In our phenomenological RHD model of the Megaflare decay phase, chromospheric condensations develop from high-flux electron beam heating in new kernels in the leading edge of spreading flare ribbons in the decay phase of the spatially integrated flux. The filling factors of the visible stellar hemisphere for each flux component are similar between the RHD models and the previous phenomenological models.

During the secondary flare of the Megaflare, a hot spot with a Vega-like flux component is formed by relativistic electron beam heating in our RHD, three-component multithread model, which accounts for the observed changes in line broadening, line decrements, and continuum flux ratios through the secondary flare. If fully relativistic electron beams are present in these types of secondary flares, (triggered) ALMA observations may be able to detect the synchrotron radiation. Adding a hotspot spectrum to the spatially superposed model of the impulsive-type dMe flares may also explain the spectrum continuum flux ratios and Balmer decrement in the main peak of these flares. Observations for the main peak in the Megaflare are not available, but these models can be applied to other large events with spectral coverage, such as the YZ CMi "Ultraflare" (Kowalski et al. 2016) or the IF3 event from Kowalski et al.

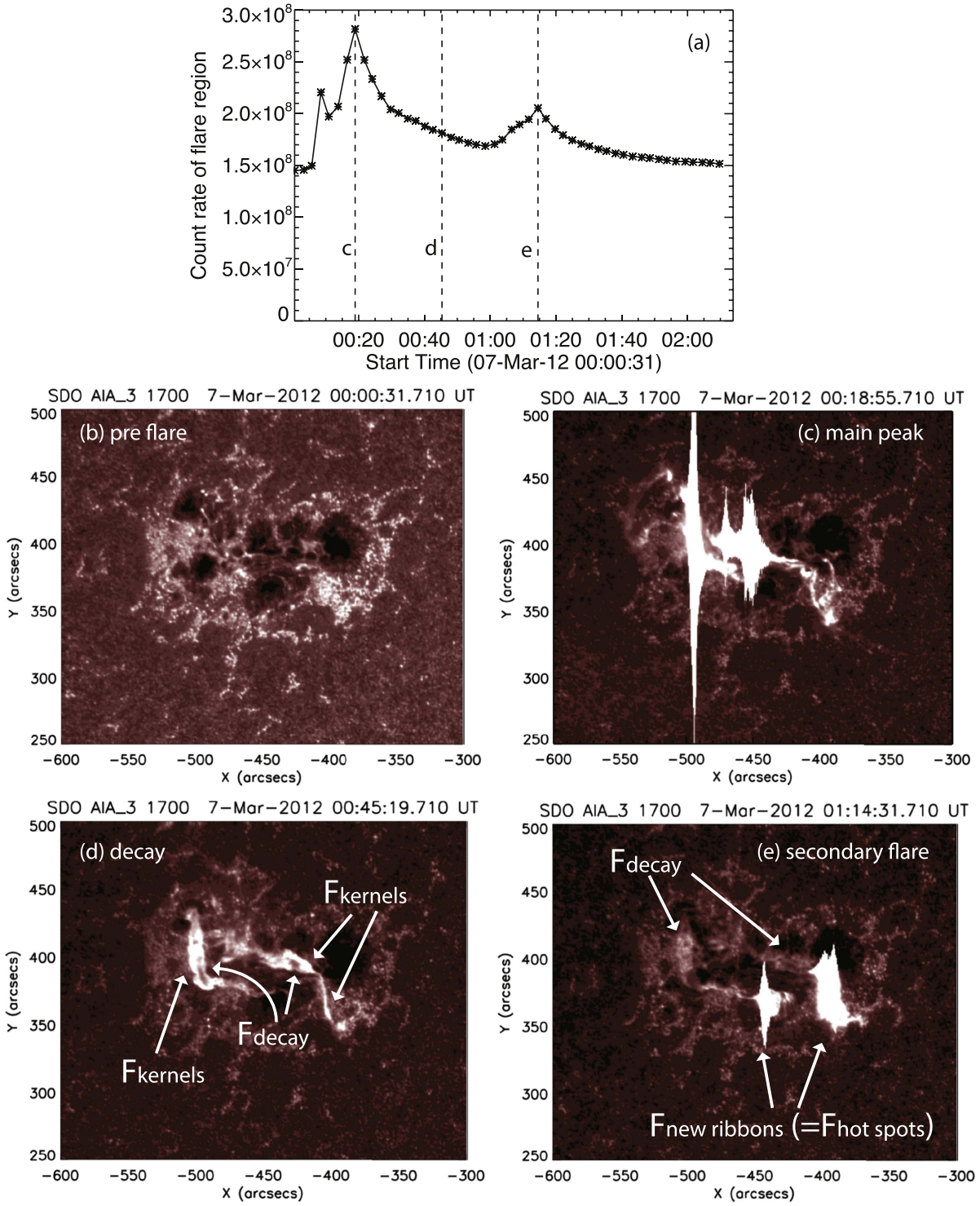

Figure 11. (a) Spatially integrated *SDO*/AIA 1700 light curve of the X-class flares on 2012 March 7 (*GOES* classes X5.4 and X1.3 peaking at 00:24 and 1:14, respectively). Panels (b)–(e) show the spatial evolution of the intensity at representative times indicated by the vertical dashed lines in (a). Panel (c) shows that two bright ribbons develop and result in brightest intensity during the main peak that saturate the image. Panel (d) shows the flare region as the light curve decays and the ribbons separate; new kernels develop as these ribbons separate from one another. As the western ribbon spreads toward the plage near the main umbra, another two-ribbon event commences; the peak of this event is shown in panel (e). The separating ribbons in (d) have decayed in brightness in (e). We interpret the three model component surface flux spectra (Figure 9) in the YZ CMi Megaflare starting ∼70 minutes after the flare start using the spatial morphology in this solar flare: (1) separating ribbons consisting of newly heated flare kernels ($F_{\rm kernels}$) at the leading edge of the ribbons, (2) decaying kernels ($F_{\rm decay}$) from each large event in the wake of the newly heated kernels, and 3) a new series of two ribbons that develop ($F_{\rm newribbons}$). In the Megaflare secondary flare MDSF2, we infer that the heating occurs at high column mass in the kernels in these new ribbons, which we refer to as hotspots ($F_{\rm hotspot}$). Several potentially analogous features in the development of the 2012 March 7 flare are indicated. Our model for S#24 in the Megaflare suggests a spatial development as in panel (d), and our model for S#113 suggests a spatial development as in panel (e) but with kernels still continuing to develop either in the new ribbons or at the leading edge of the decaying ribbons. At the approximate location of the secondary flare (panel e), there was flare activity at the time of the main flare peak. The same image scaling is used in panels (c)–(e), and *aia_prep* was used to generate these data.

(2013). The model spectra ($F_{\rm kernels}$, $F_{\rm decay}$, $F_{\rm hotspot}$) will be available online for future modeling work.

An alternative explanation for the hotspot may be heating from MeV proton beams that are preferentially accelerated in the secondary flares. MeV protons are expected to penetrate deeper than deka-keV electrons (Zharkova & Zharkov 2007) and are also thought to be preferentially accelerated in the later phases of a flare when the reconnected loops have lower magnetic field strengths (Petrosian & Liu 2004). Gamma-rays are produced from the interaction of accelerated protons, alpha particles, and ions with the solar atmosphere (Vilmer et al. 2011). Gamma-ray imaging of a gradual phase of a large solar flare has shown that the protons are preferentially accelerated in different loops than the bulk of the electrons (Hurford et al. 2006). The secondary flare peaking at 1:15 UT in Figure 11 produced hard X-ray and gamma-rays detected by *Fermi*/GBM and the *Fermi*/LAT, and the flux detected by the latter was interpreted as evidence of high-energy protons interacting with the lower atmosphere (Ajello et al. 2014). Gamma-rays are too faint to observe from other stars, but there has been a claimed detection of charge exchange from proton beams during a flare in the dMe star AU Mic (Woodgate et al. 1992). Nonthermal protons and ions are produced in solar flares with comparable energies to the nonthermal electrons (Emslie et al. 2012), and further work should be dedicated to understanding the heating from high-energy protons in solar and stellar flares, and in the (possible) role of neutralizing the F13 electron beams that we use to produce dense, chromospheric condensations. Without charge neutralization, large return current electric fields and beam instabilities would limit the propagation of F13 beams.

6.1. Speculation on the Origin of the Extended Gradual Decay Phase Component

The Hα/Hγ and Hβ/Hγ decrements are not well-reproduced by the 0–5 s average (multithread model) using the F13 because a high optical depth over the continuum-emitting regions leads to an optical depth in these lower order lines that is very large. A larger filling factor of the F13 flux at $t = 4$ s (after the beam heating ends) compared to the impulsively heated kernels is required to produce a better match to the line flux ratios.

The large filling factor (1%–2% of the visible stellar hemisphere in the Megaflare) suggests that this missing component is due to the decaying flux from previous, larger events (e.g., the main event, or the secondary flare just prior to the spectral observations). However, the timescale of the flux decay in the models ($\sim$seconds) is far too short to explain the gradual decay of flux occurring $\sim$70 minutes after the main peak of the Megaflare. Longer timescales after beam heating ends in any given kernel are needed to reproduce the timescales of the extended gradual decay phase white-light emission component in megaflares and in lower energy, classical flares (Davenport et al. 2014).

Several heating mechanisms have not yet been critically tested with RHD models and could have an important role in producing extended gradual decay phase flux. We speculate that 3D backwarming from X-rays and/or UV/EUV (300–3000 Å) line emission ("the metal line backheating hypothesis"; Machado et al. 1989; Hawley & Fisher 1992; Fisher et al. 2012) will help to account for the missing flux in the Ca II K line, the flux in the Balmer lines, and the Balmer decrement for the models. The models of Hawley & Fisher (1992) have shown that irradiation from X-rays can heat the chromosphere and produce a large ratio of emergent line-to-continuum flux. The Fe II flux in the NUV becomes bright in dMe flares (Hawley & Pettersen 1991; Hawley et al. 2007) and may also contribute significantly to the backwarming. Three-dimensional backwarming from UV/EUV lines has recently been discussed as a source of the slowly decaying component in optical flare kernels (Kawate et al. 2016). Extending the results from 1D modeling of backwarming from Balmer continuum photons (Allred et al. 2006) to 3D may also explain the observations (Metcalf et al. 1990).

After a period of fast retraction from magnetic reconnection, flare loops are expected to continue to slowly contract (Longcope & Guidoni 2011); betatron acceleration of particles in these loops may also contribute as a heating source in the extended gradual phase. Alfvén waves are expected to carry Poynting flux and heat the chromosphere with a delay from reconnection that is inversely proportional to magnetic field strength (Fletcher & Hudson 2008; Reep & Russell 2016). Our line broadening prescription will be incorporated into the publicly available version of the RH code and will be available to test the line decrement and broadening predictions from radiative-hydrodynamic multithread modeling of high-flux density electron (and proton/ion) beam heating combined with each of these additional heating scenarios. The effects of nonthermal collision rates on the Balmer line wings (Canfield & Gayley 1987; Kašparová et al. 2009) may also be revisited with the new prescription for electric pressure broadening in order to constrain the beam fluxes in the newly formed kernels. Modeling of the red-wing asymmetry in solar flares (Ichimoto & Kurokawa 1984; Sharykin & Kosovichev 2014) will also benefit by the new broadening modeling of the hydrogen wings.

7. Summary and Conclusions

Using the TB09+HM88 line profiles, we have incorporated the VCS theory of electron/proton pressure broadening into the RH code for accurate modeling of the broadening of the hydrogen lines during flares. This resolves the approximately order-of-magnitude discrepancy in the inferred ambient charge density from Balmer line broadening discussed extensively by Johns-Krull et al. (1997). Convolving the Voigt profile function with the theoretical profiles of TB09+HM88 extended from the VCS unified theory produces much broader Balmer lines than using a Voigt profile with an electric pressure damping parameter from the analytic approximations of S78. The wavelength-integrated line fluxes of Balmer lines can be several times larger with the TB09+HM88 profiles. The $\lambda > 3700$ Å spectrum calculated with our method produces a spectrum of Vega that is much more consistent with the observations of the broadening and higher order line merging than with the S78 prescription previously used in RH. Combined with the opacity effects from level dissolution at the Balmer edge, the new modeling prescription with the theoretical TB09+HM88 profiles provides self-consistent, robust constraints on flare heating model predictions for the flare-enhanced charge density in the lower atmosphere. Identifying the highest order, undissolved Balmer line resolves ambiguity in the charge density inferred from the broadening in the far wings of lower order Balmer lines, which is model dependent. Although our method for calculating the opacity effects from level dissolution is sufficient for our purposes here,

we re-iterate the suggestion of Kowalski et al. (2015b) to include the occupational probability formalism of Hubeny et al. (1994) in the non-equilibrium rate equation as new flare codes (or significant improvements to existing flare codes) are developed in the future.

We revisited the phenomenological model of the YZ CMi Megaflare with the new broadening prescription and new RHD models. A superposition of three emitting regions is necessary to reproduce the general range of values and the evolution of the Balmer decrements, broadening, and continuum flux ratios:

1. a flux component (filling factor of 0.1%) from downward-directed, heated compressions (condensations) that result from high-flux density electron beams heating the upper chromosphere in many simultaneously heated and cooling flare loops (threads);
2. a flux component (filling factor of 0.1%) from ultra-relativistic electron beam heating at high column mass (near the lower pre-flare chromosphere); and
3. a flux component (filling factor of 1%–2%) with bright, narrow line flux that decays on a longer timescale than currently produced in the models.

The flux components from #1 and #2 result from atmospheric heating to $T = 12{,}000$–$13{,}000$ K at high column mass $\sim$0.01–0.05 g cm^{-2}, at heights from $z \sim 150$–250 km (corresponding to the lower chromosphere in the pre-flare atmosphere). These two heating simulations largely differ in the hydrodynamics; most of the continuum intensity forms over a narrow (several kilometer) region in the chromospheric condensation in heating scenario #1 (Kowalski et al. 2015b), whereas the continuum intensity in heating scenario #2 forms over a 100 km uncompressed region at high column mass. The Balmer line radiation in the emergent flux spectra forms over large optical depth and high electron density in these new RHD flare models. Correct modeling of these profiles therefore requires an accurate treatment of the far wing broadening, such as that given by the VCS theory as implemented in Tremblay & Bergeron (2009). The charge density values that produce the broadening of the Balmer lines in the superposed model spectra span a large range of $n_e \sim 10^{14} - 5 \times 10^{15}$ cm^{-3}; the densities that broaden a Balmer line vary as a function of wavelength due to the optical depth variation over a line and due to the time-evolution of n_e in each model. In the superposed flux spectra models of the YZ CMi Megaflare, we require more emission line flux in the Ca II K and Balmer lines, which is evidence that flux component #3 needs improvement or that an additional component is required to produce heating over an area of the star with lower charge density than #3; one possible heating source is 3D radiative backheating.

In solar flares, the broadening evolution on several second timescales in spatially resolved kernels can be constrained with future spectral observations with the DKIST. As shown from the modeling of the YZ CMi Megaflare, spatially resolved spectra of the hydrogen lines and hydrogen edge wavelength regions during large solar events would place strong constraints on the variation of the charge density and heating mechanisms across flare ribbons.

We thank an anonymous referee for helpful comments on the manuscript and for important insights about future directions in flare research using the new broadening modeling. A.F.K. thanks Dr. G. Cauzzi for helpful discussions on flare ribbon development in DST/IBIS data and Dr. D. Graham for helpful discussions on flare area calculations. A.F.K. thanks Drs. L. Fletcher and H. Hudson for helpful discussions on line broadening while at the University of Glasgow. A.F.K. thanks Dr. H. Ludwig for pointing out white-dwarf modeling papers at Dr. S. Wedemeyer's workshop at the International Space Science Institute in Bern, Switzerland. A.F.K. acknowledges funding that supported this work from the NASA Heliophysics Guest Investigator Grant NNX15AF49G, funding from the University of Maryland Goddard Planetary Heliophysics Institute (GPHI) Task 132, and funding from *HST* GO 13323. Support for program #13323 was provided by NASA through a grant from the Space Telescope Science Institute, which is operated by the Association of Universities for Research in Astronomy, Inc., under NASA contract NAS 5-26555. S. Brown is grateful for the support of STFC Quota Studentship ST/M503502/1.

Appendix A
High E_c RHD Flare Models

As discussed in Kowalski et al. (2016), we are working on a large grid of RADYN flare models where we vary the parameters of the nonthermal electron beam and have found that models with a high value of E_c cause the beam energy to penetrate deeper than values near 20–37 keV, which are typical values in solar flares. High E_c models also contain fewer electrons for the same energy flux as lower E_c models, and thus there are smaller effects from the return current and beam instabilities. Here we describe two representative models from our grid of dMe flare models that reproduce key properties of dMe white-light continuum flux and have important differences in the broadening and decrements of flare spectra than lower E_c models.

A.1. The Starting Atmosphere

We update the starting dMe pre-flare atmosphere from Kowalski et al. (2015b) using the prescription for incident XUEV radiation described in Allred et al. (2015). Charge conservation is calculated using the ionization from the detailed elements hydrogen and helium, but for calcium the electron contribution to charge conservation is calculated from LTE (as for the remaining elements). In future work, we intend to include a Ca I–II–III model atom in RADYN that is appropriate for the NLTE ionization and charge contribution for an M dwarf atmosphere (in the Sun, Ca II is dominant and a calcium ion without the neutral stage is sufficient for the detailed losses in RADYN). For atoms and ions not treated in detail, we use the radiative loss function from Allred et al. (2015), which includes the most updated losses from CHIANTI at $T > 20{,}000$ K but excludes several ions at low temperature at $T < 20{,}000$ K that are optically thick in flares (e.g., Fe II, Si II, Mg II, Al II) as discussed by Ricchiazzi & Canfield (1983) and Hawley & Fisher (1992). We converge the atmosphere top boundary that is reflecting with a zero temperature gradient. We also apply a small amount of non-radiative heating (0.23 erg cm^{-3} s^{-1}) to all heights with $T > 1$ MK for a temperature gradient in the corona that produces a transition from conductive cooling to conductive heating at the transition region (Klimchuk et al. 2008). The atmosphere is relaxed with this condition and this heating is applied through the flare simulations to keep the corona from cooling below the pre-flare

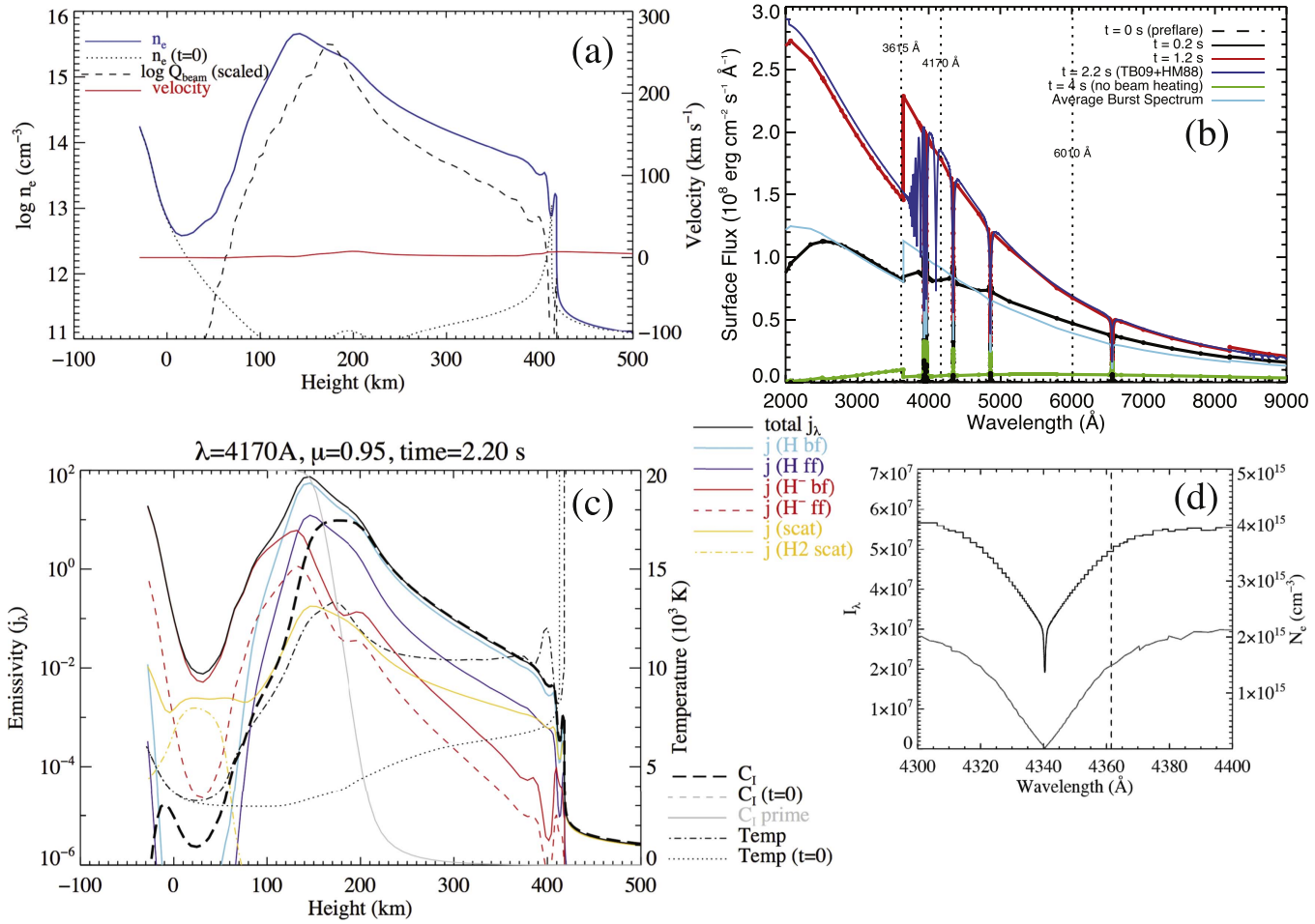

Figure 12. (a) Electron density vs. height at $t = 2.2$ s in the $E_c = 500$ keV heating model. The volumetric beam heating ($Q_{\rm beam}$; erg cm^{-3} s^{-1}) is shown scaled to the left axis over 5 dex. (b) The evolution of the detailed flux spectrum from RADYN at $t = 0$, 0.2, 1.2 and 4 s; the spectrum from RH at $t = 2.2$ s is shown with the TB09+HM88 broadening and the opacity from level dissolution. (c) Sources of continuum emissivity that contribute to the emergent continuum intensity at $\lambda = 4170$ Å at $t = 2.2$ s in the $E_c = 500$ keV heating model. The contribution function (thick dashed line) to the emergent intensity and the cumulative contribution function (gray; C_I') show that the continuum is formed over a "hot spot" with a peak temperature of nearly 13,000 K. The dominant source of emissivity over the hot spot is spontaneous hydrogen recombination (bound-free, bf) emissivity. (d) The emergent intensity at $\mu = 0.95$ for the Hγ line with the TB09+HM88 broadening (black line); the contribution-function-weighted electron density is shown on the right axis (gray line), and a vertical dashed line indicates the same wavelength in the far red wing in Figure 4 (bottom).

temperature. We also note that the chemical equilibrium of hydrogen and H_2 is included using LTE dissociation, which is important in the photosphere. Continuum wavelengths that have been added to the detailed radiative transfer are $\lambda = 1332$, 1358, 1389, 1407, 1435, 1610, 2519, 2671, 2780, 2826, 3300, 3500, 3615, 4170, and 6010 Å. These are needed for direct comparisons to data.

A.2. The $E_c = 500$ keV Flare Model

We apply electron beam heating for 2.3 s with $E_c = 500$ keV, $\delta = 7$, and an energy flux density of 2×10^{12} erg cm^{-2} s^{-1} (2F12). The atmosphere is allowed to relax for 60 s after 2.3 s. These parameters were chosen so that the beam energy is localized to the lower atmosphere and results in a local temperature maximum near $T \sim 10{,}000$ K within a short time to be consistent with the short pulses observed during solar and dMe flares (Aschwanden et al. 1995; Robinson et al. 1995).

In Figure 12, we show the physical parameters at $t = 2.2$ s in the lower atmosphere: the electron density variation, gas velocity, and beam heating in panel (a) the emergent flux spectra at representative times ($F_{\rm hotspot}(t)$; see the text) in panel (b), the contribution function to the emergent continuum intensity and the continuum emissivity processes at $\lambda = 4170$Å in panel (c) using the method described in Kowalski et al. (2017), and an inset of the Hγ line with the TB09+HM88 broadening calculated from RH in panel (d). The gray line in panel (c) shows the cumulative contribution function (C_I') normalized from 0 to 1 on the right axis, which illustrates the depth range over which the emergent intensity is formed. The blue ($\lambda = 4170$ Å) continuum forms over $z = 150$–235 km, which corresponds to a log column mass range of log $m/$g cm$^{-2} = -1.26$ to -2.05, a large range of electron density from $(5 - 40) \times 10^{14}$ cm^{-3} (with a contribution-function-weighted average of 2.3×10^{15} cm^{-3}), and a temperature range from $T = 10{,}800$–12,700 K. The electron density weighted by the contribution function for the emergent intensity over the Hγ line ranges from 2×10^{13} cm^{-3} at line center to 1.8×10^{15} cm^{-3} in the far wing ($\lambda_{\rm rest} + 20$ Å). The broadening is comparable to the Vega spectrum of Hγ, which forms over an electron density range that is significantly lower ($n_e = 10^{12}$ cm^{-3} at line center and only 5×10^{14} cm^{-3} in the far wings). Vega has a factor of nearly 100 lower gravity

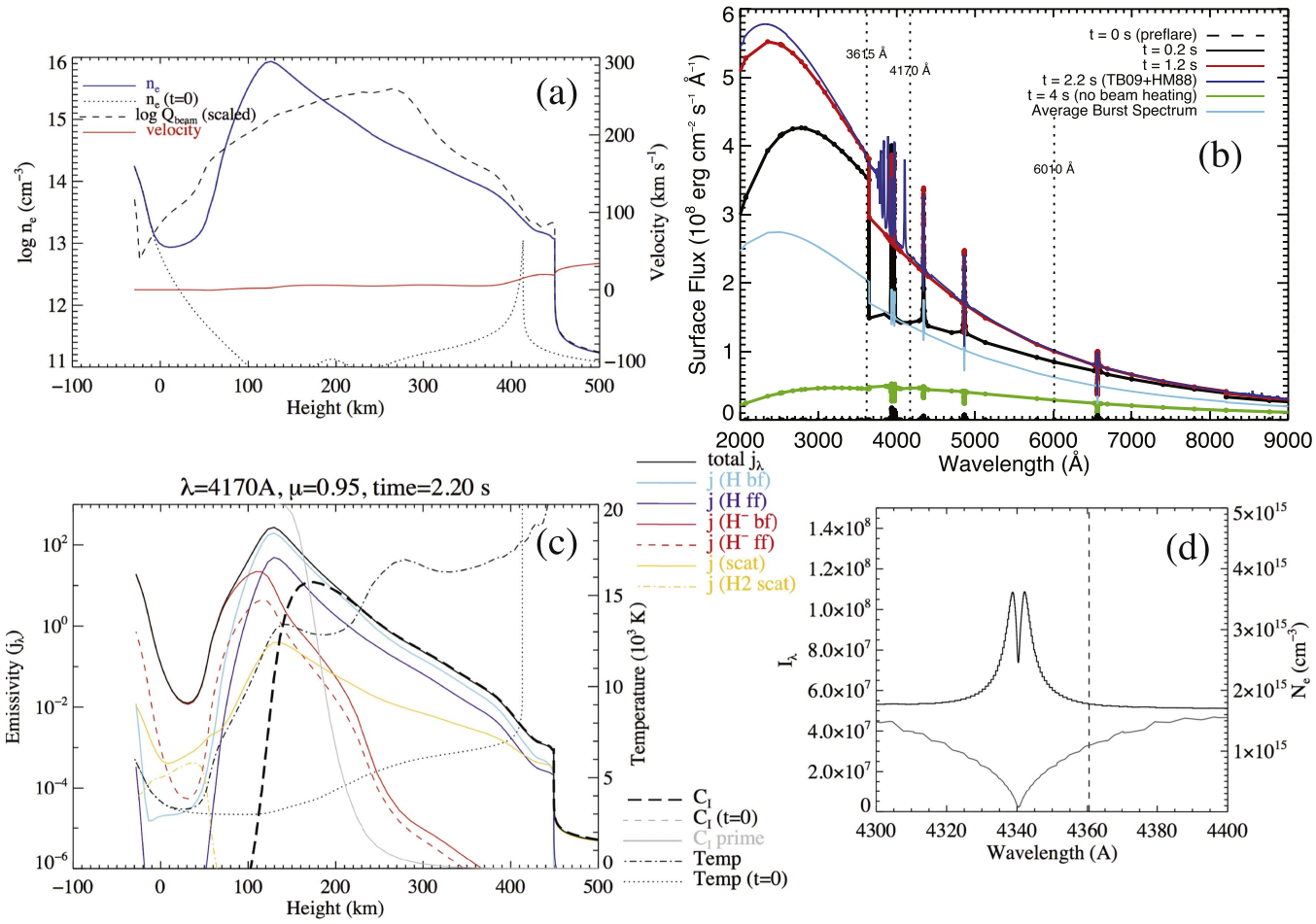

Figure 13. We show the same panels as in Figure 12 for the $E_c = 150$ keV, $\delta = 3$, 5F12 electron beam heating model.

compared to the M dwarf, and thus the radiation is formed over ∼1000–2000 km in the line wing (Figure 4) compared to 85 km in the line wing of the M dwarf $E_c = 500$ keV model. Thus, a comparable opacity is produced over a larger range of heights with lower density in Vega. In the Balmer edge region, the highest order undissolved Balmer line in absorption is ≈H13 in the $E_c = 500$ keV model (Figure 9), whereas in the Vega model (Figure 3 top) it is H16 or higher, as expected from the density dependence on the occupational probability of higher levels (see Figure 9 of Kowalski et al. 2015b).

Using the equations in Holman (2012) for the energy lost due to the return current electric field (assuming that proton beams do not neutralize the electron beam), the energy lost over the top 8 Mm of the corona is 4 keV/electron and the Joule heating rate is ∼15 erg cm^{-3} s^{-1}. The 500 keV electrons lose a small fraction of their initial energy and thus we do not expect the beam spectrum to be modified significantly. The coronal heating rate from the return current is 65× the heating rate necessary to keep the pre-flare corona hot. This compares to nearly 8000 erg cm^{-3} s^{-1} that results from an F13 beam with $E_c = 37$ keV and $\delta = 3$. The return current drift speed is <10% of the electron thermal speed in the corona, and therefore we do not expect energy-draining double-layers to develop (Lee et al. 2008; Li et al. 2014); for the F13 beam the drift speed is three times the electron thermal speed and double layers will form.

A.3. The $E_c = 150$ keV Flare Model

We apply electron beam heating for 2.3 s with $E_c = 150$ keV, $\delta = 3$, and an energy flux density of 5×10^{12} erg cm^{-2} s^{-1} (5F12). The atmosphere is allowed to relax for 60 s after 2.3 s. For this beam, we calculate that <20 keV is lost per electron in the propagation over the top 8 Mm of the loop and there is a Joule heating rate from the return current of 350 erg cm^{-3} s^{-1} that will result in a temperature change. The drift speed of the return current is 40% of the electron thermal speed in the corona, and thus we do not expect energy-draining double-layers to develop (Lee et al. 2008; Li et al. 2014).

The model results are shown in Figure 13 for the same panels as for the $E_c = 500$ keV model in Appendix A.2. Compared to the phenomenological models of Cram & Woods (1982), the temperature profile, density, and emergent continuum spectrum are similar to the extreme model #5, whereas the broad Balmer wings with deep central reversals are similar to the emergent Hα profile from model #3 that exhibits a low column mass transition region. In the $E_c = 150$ keV model, the transition region is at low column mass as in the Cram & Woods (1982) model #3, but the temperature and electron density values at high column mass (log m/g cm^{-2} = −2) are larger than the Cram & Woods (1982) model #5.

Compared to the 2F12, $E_c = 500$, $\delta = 7$ heating model (Appendix A.2), the blue ($\lambda = 4170$ Å) continuum forms over

comparable heights ($z \sim 150$–250 km; see the C_I' curves), column masses ($\log\ m/\mathrm{g\ cm^{-2}} > -2.2$), temperatures ($\sim$12,000–13,000 K), and electron densities ($n_e = 5$–$40 \times 10^{14}\,\mathrm{cm^{-3}}$ with the same contribution function-weighted electron density of $2.3 \times 10^{15}\,\mathrm{cm^{-3}}$). The relative importance of each emissivity process in the formation of the continuum intensity (panel (c) in Figures 12 and 13) is very similar for the two models, while the contribution function-weighted electron density over the Hγ lines (panel d in Figures 12 and 13) is also similar. In both heating simulations, the formation of the emergent continuum intensity at $\lambda = 3615$ Å is shifted 50 km higher than the formation of the $\lambda = 4170$ Å emergent continuum intensity because of the larger Balmer ($n = 2 \rightarrow \infty$) bound–free opacity compared to the Paschen ($n = 3 \rightarrow \infty$) bound–free opacity. As a result, the $\lambda = 3615$ Å emergent continuum intensity originates from a lower electron density than the $\lambda = 4170$ Å continuum intensity. This produces much smaller Balmer jump ratios (F_{3615}/F_{4170}) in the model spectra than for a spectrum that results from hydrogen recombination over low optical depth. In contrast, the F13 model spectra exhibit small Balmer jump ratios because of the large variation of the physical depth range as a function of wavelength, as described in Kowalski et al. (2015b, 2016) and Kowalski (2015). The F13 model also has two flaring layers with an electron density profile that increases outward, in contrast to the high E_c models, which exhibit electron density profiles that increase toward lower heights. The electron density variation over the two flaring layers combined with the optical depth variation (resulting in the physical depth range variation) as a function of wavelength both contribute to the characteristics of the emergent flux spectrum in the F13 model.

The striking differences in the emergent flux and intensity spectra of the Balmer lines and at wavelengths in the Balmer continuum for the $E_c = 150$ and $E_c = 500$ keV models can be explained with the panels in Figures 12 and 13. The lower energy cutoff ($E_c = 150$ keV) heats the mid and upper chromosphere to a much larger extent than the $E_c = 500$ keV model; the beam heating peaks at $z \sim 280$ km in the former and at $z \sim 180$ km in the latter (panel a of Figures 12 and 13). The larger heating rates at $z > 250$ km in the $E_c = 150$ keV model produce a larger ionization fraction and excitation at these heights, which leads to a lower optical depth in the Balmer continuum and Balmer lines. For example, $\tau_{3615} = 1$ occurs at $z = 210$ km in the $E_c = 150$ keV model and at $z = 225$ km in the $E_c = 500$ keV model. For the emergent Balmer continuum flux (e.g., $\lambda = 3615$ Å) in the $E_c = 150$ keV model, the photons are formed deeper and at higher n_e: at $\tau_{3615} = 1$ the electron density ($1.3 \times 10^{15}\,\mathrm{cm^{-3}}$) is 1.8x larger than the density ($7 \times 10^{14}\,\mathrm{cm^{-3}}$) at $\tau_{3615} = 1$ in the $E_c = 500$ keV model, which results in a larger continuum emissivity ($\propto n_e^2$) at the heights where $\tau_{3615} = 1$ and a larger emergent continuum flux. Therefore, the emergent Balmer continuum flux in the $E_c = 150$ keV model is relatively brighter than the $\lambda = 4170$ Å flux (the Balmer continuum flux is "in emission") whereas the Balmer continuum flux in the $E_c = 500$ keV is fainter than the $\lambda = 4170$ Å continuum flux (the Balmer continuum flux is "in absorption"). The formation of the $\lambda = 4170$ Å continuum flux is similar in the two models because the $E_c = 150$ keV model has a very hard distribution ($\delta = 3$) and a higher flux, which heats the deeper layers to a comparable level as the softer, lower flux, higher-energy $E_c = 500$ keV model.

At $\lambda_{\mathrm{rest}} + 2.5$ Å, the $E_c = 150$ keV model Hγ intensity is in emission while the $E_c = 500$ keV model Hγ intensity is in absorption. Although the electron density for the line formation appears similar in panel (d) of Figures 12 and 13, there is a factor of 1.5× larger electron density for the $E_c = 150$ keV model at $\lambda_{\mathrm{rest}} + 2.5$ Å. Because of the higher temperature at $z > 200$ km, the optical depth is lower in the line and Hγ is formed deeper where there is higher electron density. The higher temperature over the line formation for the $E_c = 150$ keV model also contributes to a larger emergent intensity because n_u for Hγ has a larger population density due to the scaling of the collisional rates with temperature via the Boltzmann exponential factor (n_u and n_l for Hγ are near LTE at the height of the maximum in the contribution function in these models).

Appendix B
Terminology and Abbreviations

In this appendix, we show a list of abbreviations and terminology used throughout the text.

1. *MDSF2*: "Megaflare Decay Secondary Flare #2" (see Figure 8).
2. *S#24*: Spectrum # 24 in the decay phase of the YZ CMi Megaflare (see Figure 8).
3. *S#113*: Spectrum # 113 at the peak of the MDSF2 event in the YZ CMi Megaflare (see Figure 8).
4. *VCS*: The unified theory of electron and proton pressure broadening presented in Vidal et al. (1971, 1973).
5. *TB09+HM88*: The profiles calculated with the VCS unified theory extended with the modifications of Tremblay & Bergeron (2009), the occupational probability formalism of Hummer & Mihalas (1988), and the non-ideal, pseudo-continuum opacity of Dappen et al. (1987).
6. *S78*: The analytic prescription for electron and proton pressure broadening from Sutton (1978) employed in the RH code using a damping parameter, Γ_S, in the Voigt function.
7. E_c: Lowest energy electron in the power-law distribution of a nonthermal electron beam.
8. *F13*: Nonthermal electron beam energy flux density of $10^{13}\,\mathrm{erg\,cm^{-2}\,s^{-1}}$ and $E_c = 37$ keV.
9. *F13 dpl*: F13 heating simulation from Kowalski et al. (2015b) with a double-power-law electron beam distribution parameterized by $\delta = 3$ at $E < 105$ keV and $\delta = 4$ at $E > 105$ keV.
10. *F13* $\delta = 3$: F13 flare simulation from Kowalski et al. (2016) with a single-power-law (spl) electron beam distribution parametrized by a power-law index of $\delta = 3$.
11. *C3615*: The flare continuum specific flux averaged over $\lambda = 3600$–3630 Å.
12. *Hγ/C4170*: The line-integrated flare flux in Hγ divided by the flare continuum specific flux averaged over $\lambda = 4155$–4185 Å.
13. *multithread model*: 0–5 s average (0–5 s ave) of an F13 simulation; also referred to as "average burst spectrum."
14. *DG CVn Superflare multithread model*: 0–5 s average of an F13 model in addition to the instantaneous F13 model at $t = 4$ s with a 25 times greater filling factor than the 0–5 s average F13 model.

15. *pseudo-continuum*: The non-ideal Balmer continuum opacity longward of the Balmer limit wavelength is referred to as the pseudo-continuum opacity, or dissolved level continuum opacity (referred to as L–Z Balmer continuum opacity in Kowalski et al. (2015b).

References

Abbett, W. P., & Hawley, S. L. 1999, ApJ, 521, 906
Ajello, M., Albert, A., Allafort, A., et al. 2014, ApJ, 789, 20
Allred, J. C., Hawley, S. L., Abbett, W. P., & Carlsson, M. 2005, ApJ, 630, 573
Allred, J. C., Hawley, S. L., Abbett, W. P., & Carlsson, M. 2006, ApJ, 644, 484
Allred, J. C., Kowalski, A. F., & Carlsson, M. 2015, ApJ, 809, 104
Arakelyan, A., Nunkaew, J., & Gallagher, T. F. 2016, PhRvA, 94, 053416
Aschwanden, M. J., Schwartz, R. A., & Alt, D. M. 1995, ApJ, 447, 923
Aufdenberg, J. P., Mérand, A., Coudé du Foresto, V., et al. 2006, ApJ, 645, 664
Ayres, T. R. 2015, AJ, 150, 7
Bengtson, R. D., Tannich, J. D., & Kepple, P. 1970, PhRvA, 1, 532
Bochanski, J. J., West, A. A., Hawley, S. L., & Covey, K. R. 2007, AJ, 133, 531
Bohlin, R. C. 2007, in ASP Conf. Ser. 364, The Future of Photometric, Spectrophotometric and Polarimetric Standardization, ed. C. Sterken (San Francisco, CA: ASP), 315
Bohlin, R. C., & Gilliland, R. L. 2004, AJ, 127, 3508
Bohlin, R. C., Gordon, K. D., & Tremblay, P.-E. 2014, PASP, 126, 711
Brekke, P., Rottman, G. J., Fontenla, J., & Judge, P. G. 1996, ApJ, 468, 418
Brown, J. C. 1971, SoPh, 18, 489
Canfield, R. C., & Gayley, K. G. 1987, ApJ, 322, 999
Carlsson, M. 1986, A Computer Program for Solving Multi-Level Non-LTE Radiative Transfer Problems in Moving or Static Atmospheres (Rept. No. 33; Uppsala: Uppsala Astronomical Obs.)
Carlsson, M., & Rutten, R. J. 1992, A&A, 259, L53
Carlsson, M., & Stein, R. F. 1997, ApJ, 481, 500
Castelli, F., & Kurucz, R. L. 1994, A&A, 281, 817
Castelli, F., & Kurucz, R. L. 2004, arXiv:astro-ph/0405087
Cook, J. W., & Brueckner, G. E. 1979, ApJ, 227, 645
Cram, L. E., & Woods, D. T. 1982, ApJ, 257, 269
Dappen, W., Anderson, L., & Mihalas, D. 1987, ApJ, 319, 195
Davenport, J. R. A., Hawley, S. L., Hebb, L., et al. 2014, ApJ, 797, 122
Donati-Falchi, A., Falciani, R., & Smaldone, L. A. 1985, A&A, 152, 165
Doyle, J. G., Butler, C. J., Bryne, P. B., & van den Oord, G. H. J. 1988, A&A, 193, 229
Doyle, J. G., & Cook, J. W. 1992, ApJ, 391, 393
Drake, S. A., & Ulrich, R. K. 1980, ApJS, 42, 351
Eason, E. L. E., Giampapa, M. S., Radick, R. R., Worden, S. P., & Hege, E. K. 1992, AJ, 104, 1161
Emslie, A. G. 1978, ApJ, 224, 241
Emslie, A. G., Dennis, B. R., Shih, A. Y., et al. 2012, ApJ, 759, 71
Fisher, G. H., Bercik, D. J., Welsch, B. T., & Hudson, H. S. 2012, SoPh, 277, 59
Fletcher, L., & Hudson, H. S. 2008, ApJ, 675, 1645
Fuhrmeister, B., Lalitha, S., Poppenhaeger, K., et al. 2011, A&A, 534, A133
Fuhrmeister, B., Liefke, C., Schmitt, J. H. M. M., & Reiners, A. 2008, A&A, 487, 293
García-Alvarez, D., Jevremović, D., Doyle, J. G., & Butler, C. J. 2002, A&A, 383, 548
Gizis, J. E., Burgasser, A. J., Berger, E., et al. 2013, ApJ, 779, 172
Hawley, S. L., Allred, J. C., Johns-Krull, C. M., et al. 2003, ApJ, 597, 535
Hawley, S. L., & Fisher, G. H. 1992, ApJS, 78, 565
Hawley, S. L., & Fisher, G. H. 1994, ApJ, 426, 387
Hawley, S. L., & Pettersen, B. R. 1991, ApJ, 378, 725
Hawley, S. L., Walkowicz, L. M., Allred, J. C., & Valenti, J. A. 2007, PASP, 119, 67
Heinzel, P., & Kleint, L. 2014, ApJL, 794, L23
Holman, G. D. 2012, ApJ, 745, 52
Hubeny, I., Hummer, D. G., & Lanz, T. 1994, A&A, 282, 151
Hummer, D. G., & Mihalas, D. 1988, ApJ, 331, 794
Hurford, G. J., Krucker, S., Lin, R. P., et al. 2006, ApJL, 644, L93
Ichimoto, K., & Kurokawa, H. 1984, SoPh, 93, 105
Isobe, H., Kubo, M., Minoshima, T., et al. 2007, PASJ, 59, S807
Jevremovic, D., Butler, C. J., Drake, S. A., O'Donoghue, D., & van Wyk, F. 1998, A&A, 338, 1057
Jing, J., Xu, Y., Cao, W., et al. 2016, NatSR, 6, 24319
Johns-Krull, C. M., Hawley, S. L., Basri, G., & Valenti, J. A. 1997, ApJS, 112, 221
Kašparová, J., Varady, M., Heinzel, P., Karlický, M., & Moravec, Z. 2009, A&A, 499, 923
Kawate, T., Ishii, T. T., Nakatani, Y., et al. 2016, ApJ, 833, 50
Kepple, P., & Griem, H. R. 1968, PhRv, 173, 317
Klimchuk, J. A., Patsourakos, S., & Cargill, P. J. 2008, ApJ, 682, 1351
Kowalski, A. F. 2012, PhD thesis, Univ. Washington
Kowalski, A. F. 2016, in IAU Symp. 320, Solar and Stellar Flares and their Effects on Planets (Cambridge: Cambridge Univ. Press), 259
Kowalski, A. F., Allred, J. C., Daw, A., Cauzzi, G., & Carlsson, M. 2017, ApJ, 836, 12
Kowalski, A. F., Cauzzi, G., & Fletcher, L. 2015a, ApJ, 798, 107
Kowalski, A. F., Hawley, S. L., Carlsson, M., et al. 2015b, SoPh, 290, 3487
Kowalski, A. F., Hawley, S. L., Holtzman, J. A., Wisniewski, J. P., & Hilton, E. J. 2010, ApJL, 714, L98
Kowalski, A. F., Hawley, S. L., Holtzman, J. A., Wisniewski, J. P., & Hilton, E. J. 2011, in IAU Symp. 273, Physics of Sun and Star Spots, ed. D. Prasad Choudhary & K. G. Strassmeier (Cambridge: Cambridge Univ. Press), 261
Kowalski, A. F., Hawley, S. L., Holtzman, J. A., Wisniewski, J. P., & Hilton, E. J. 2012, SoPh, 277, 21
Kowalski, A. F., Hawley, S. L., Wisniewski, J. P., et al. 2013, ApJS, 207, 15
Kowalski, A. F., Mathioudakis, M., Hawley, S. L., et al. 2016, ApJ, 820, 95
Krucker, S., Giménez de Castro, C. G., Hudson, H. S., et al. 2013, A&ARv, 21, 58
Kurochka, L. N., & Maslennikova, L. B. 1970, SoPh, 11, 33
Lee, K. W., Büchner, J., & Elkina, N. 2008, A&A, 478, 889
Leenaarts, J., Carlsson, M., & Rouppe van der Voort, L. 2012, ApJ, 749, 136
Lemen, J. R., Title, A. M., Akin, D. J., et al. 2012, SoPh, 275, 17
Lemke, M. 1997, A&AS, 122, 285
Li, T. C., Drake, J. F., & Swisdak, M. 2014, ApJ, 793, 7
Longcope, D. W. 2014, ApJ, 795, 10
Longcope, D. W., & Guidoni, S. E. 2011, ApJ, 740, 73
Machado, M. E., Emslie, A. G., & Avrett, E. H. 1989, SoPh, 124, 303
Massi, M., Forbrich, J., Menten, K. M., et al. 2006, A&A, 453, 959
Metcalf, T. R., Canfield, R. C., & Saba, J. L. R. 1990, ApJ, 365, 391
Mihalas, D. 1978, Stellar Atmospheres (2nd ed.; San Francisco, CA: W.H. Freeman and Co.)
Osten, R. A., Kowalski, A., Drake, S. A., et al. 2016, ApJ, 832, 174
Paulson, D. B., Allred, J. C., Anderson, R. B., et al. 2006, PASP, 118, 227
Perotti, L. 2006, PhRvA, 73, 053405
Petrosian, V., & Liu, S. 2004, ApJ, 610, 550
Phillips, K. J. H., Bromage, G. E., Dufton, P. L., Keenan, F. P., & Kingston, A. E. 1988, MNRAS, 235, 573
Pillet, P., Kachru, R., Tran, N. H., Gallagher, T. F., & Smith, W. W. 1983, PhRvL, 50, 1042
Pillet, P., van Linden van den Heuvell, H. B., Smith, W. W., et al. 1984, PhRvA, 30, 280
Qiu, J., Sturrock, Z., Longcope, D. W., Klimchuk, J. A., & Liu, W.-J. 2013, ApJ, 774, 14
Reep, J. W., & Russell, A. J. B. 2016, ApJL, 818, L20
Reep, J. W., Warren, H. P., Crump, N. A., & Simões, P. J. A. 2016, ApJ, 827, 145
Ricchiazzi, P. J., & Canfield, R. C. 1983, ApJ, 272, 739
Robinson, R. D., Carpenter, K. G., Percival, J. W., & Bookbinder, J. A. 1995, ApJ, 451, 795
Rubbmark, J. R., Kash, M. M., Littman, M. G., & Kleppner, D. 1981, PhRvA, 23, 3107
Rubio da Costa, F., Kleint, L., Petrosian, V., Liu, W., & Allred, J. C. 2016, ApJ, 827, 38
Russell, A. J. B., & Fletcher, L. 2013, ApJ, 765, 81
Seaton, M. J. 1990, JPhB, 23, 3255
Sharykin, I. N., & Kosovichev, A. G. 2014, ApJL, 788, L18
Stoneman, R. C., Thomson, D. S., & Gallagher, T. F. 1988, PhRvA, 37, 1527
Sutton, K. 1978, JQSRT, 20, 333
Svestka, Z. 1962, BAICz, 13, 236
Svestka, Z. 1963, BAICz, 14, 234
Švestka, Z., & Fritzová-Švestková, L. 1967, SoPh, 2, 75
Tremblay, P.-E., & Bergeron, P. 2009, ApJ, 696, 1755
Uitenbroek, H. 2001, ApJ, 557, 389
Uitenbroek, H., & Criscuoli, S. 2011, ApJ, 736, 69
Vidal, C. R., Cooper, J., & Smith, E. W. 1970, JQSRT, 10, 1011
Vidal, C. R., Cooper, J., & Smith, E. W. 1971, JQSRT, 11, 263
Vidal, C. R., Cooper, J., & Smith, E. W. 1973, ApJS, 25, 37

Vilmer, N., MacKinnon, A. L., & Hurford, G. J. 2011, SSRv, 159, 167
Walkowicz, L. M. 2008, PhD thesis, Univ. Washington
Warmuth, A., Holman, G. D., Dennis, B. R., et al. 2009, ApJ, 699, 917
Warren, H. P. 2006, ApJ, 637, 522
Wedemeyer, S., & Ludwig, H.-G. 2016, in IAU Symp. 320, Solar and Stellar Flares and their Effects on Planets (Cambridge: Cambridge Univ. Press), 303
Woodgate, B. E., Robinson, R. D., Carpenter, K. G., Maran, S. P., & Shore, S. N. 1992, ApJL, 397, L95
Worden, S. P., Schneeberger, T. J., Giampapa, M. S., Deluca, E. E., & Cram, L. E. 1984, ApJ, 276, 270
Zener, C. 1932, RSPSA, 137, 696
Zharkova, V. V., & Zharkov, S. I. 2007, ApJ, 664, 573